



Bridging the gaps between particulate backscattering measurements and modeled particulate organic carbon in the ocean

Martí Galí¹, Marcus Falls¹, Hervé Claustre², Olivier Aumont³, Raffaele Bernardello¹

¹Barcelona Supercomputing Center (BSC)

5 ²CNRS and Sorbonne Université, Laboratoire d'Océanographie de Villefranche, LOV, 06230 Villefranche-sur-7Mer, France

³Sorbonne Université (CNRS/IRD/MNHN), LOCEAN-IPSL, Paris, France

Correspondence to: Martí Galí (marti.gali.tapias@gmail.com)

Abstract. Oceanic particulate organic carbon (POC) is a relatively small (~4 Pg C) but dynamic component of the global carbon cycle with fast mean turnover rates compared to other oceanic, continental and atmospheric carbon stocks. Biogeochemical models historically focused on reproducing the sinking flux of POC driven by large fast-sinking particles (bPOC). However, suspended and slow-sinking particles (sPOC) typically represent 80–90% of the POC stock, and can make important seasonal contributions to vertical fluxes through the mesopelagic layer (200–1000 m). Recent developments in the parameterization of POC reactivity in the PISCES model (PISCESv2_RC) have greatly improved its ability to capture sPOC dynamics. Here we evaluated this model by matching 3D and 1D simulations with BGC-Argo and satellite observations in globally representative ocean biomes, building on a refined scheme for converting particulate backscattering profiles measured by BGC-Argo floats to POC. We show that PISCES captures the major features of sPOC and bPOC as seen by BGC-Argo floats across a range of spatiotemporal scales, from highly resolved profile time series to biome-aggregated climatological profiles. Our results also illustrate how the comparison between the model and observations is hampered by (1) the uncertainties in empirical POC estimation, (2) the imperfect correspondence between modelled and observed variables, and (3) the bias between modelled and observed physics. Despite these limitations, we identified characteristic patterns of model-observations misfits in the mesopelagic layer of subpolar and subtropical gyres. These misfits likely result from both suboptimal model parameters and model equations themselves, pointing to the need to improve the model representation of processes with a critical influence on POC dynamics, such as sinking, remineralization, (dis)aggregation and zooplankton activity. Beyond model evaluation results, our analysis identified inconsistencies between current estimates of POC from satellite and BGC-Argo data, as well as POC partitioning into phytoplankton, heterotrophs and detritus deduced from in situ bio-optical data. Our approach can help constrain POC stocks, and ultimately budgets, in the epipelagic and mesopelagic ocean.



30 **1 Introduction**

The biological carbon pump (BCP) is the ensemble of processes that transfer the organic matter produced by plankton in the sunlit ocean surface to deeper layers (Volk and Hoffert, 1985). This vertical flux plays a central role in the Earth's climate, as it influences the oceans' capacity to absorb and ultimately store atmospheric CO₂ over centennial or millennial time scales (Kwon et al., 2009). The BCP is also central to biogeochemical functioning of the ocean, as it determines the quality and
35 quantity of organic matter available to the ocean interior (Aristegui et al., 2009; Hernández-León et al., 2020) and the seafloor. Organic matter respiration in the ocean interior influences the distribution of oxygen, inorganic carbon and remineralized nutrients (Duteil et al., 2012; Oschlies et al., 2018; Weber et al., 2016), and their return pathways to the surface. Sinking particles are also efficient trace metal scavengers (Hayes et al., 2015). In consequence, the BCP is intimately linked to, and feeds back on, upper ocean productivity.

40 Over the last decades, BCP research has placed emphasis on understanding the ecological and physical factors that control export efficiency (the fraction of net primary production exported below the euphotic layer) and transfer efficiency (Teff; the fraction of export production that reaches a given depth below the euphotic layer), both of which vary widely across ocean biomes and along the seasonal cycle (Buesseler and Boyd, 2009; Buesseler et al., 2020). Therefore, biogeochemical models
45 have been built, and their parameters tuned, to be able to reproduce sparse observations of export production and vertical carbon flux attenuation (Guidi et al., 2015; Henson et al., 2011; Laws et al., 2000), sometimes reaching apparently contradictory results (Marsay et al., 2015). In comparison, the models' ability to represent marine particle concentrations has received less attention (Lam et al., 2011).

50 Marine particles are mainly composed of living microbial plankton cells, living metazoans and detritus ("marine snow" aggregates, fecal pellets, zooplankton feeding structures), whose size ranges from <1 μm to several mm (Stemmann and Boss, 2012). Indeed, these particles also feature wide variations in shape, density, chemical composition and reactivity towards microbial degradation (Kharbush et al., 2020). Building on the overall increase in gravitational sinking speed with
55 particle size (Cael and White, 2020; Stemmann et al., 2004a), particle populations are usually partitioned into a few functional size classes: big particles, typically defined as larger than 50 or 100 μm, which sink at several tens or hundreds of m d⁻¹; and small particles, including suspended and slow-sinking (<10 m d⁻¹) particles. In this study, the particulate organic carbon (POC) is divided into small POC (sPOC) and big POC (bPOC), with a nominal cutoff at 100 μm (Table 1; section 2.2.2).



60 The traditional BCP paradigm posits that bPOC controls the vertical carbon flux (Sarmiento and Gruber, 2006). However, a
wider paradigm has emerged during the last decade, shifting our attention to carbon export processes other than gravitational
sinking. These processes were collectively termed “particle injection pumps”, and include both the “active flux” mediated by
the vertical migration of metazoans and the physical “particle injection pumps” resulting from oceanic convection and water-
mass subduction at various scales (Boyd et al., 2019). In parallel, the role of dissolved organic carbon in vertical carbon
65 export has been widely recognized (Jiao et al., 2010; Legendre et al., 2015).

One aspect that has recently received considerable attention is the role of suspended and slow-sinking particles. Owing to
their longer residence time, small particles represent the majority of the POC stock (Aumont et al., 2017; Baker et al., 2017)
and may support a proportional fraction of the respiration (Baltar et al., 2010a, 2010b; Belcher et al., 2016; Iversen and
70 Ploug, 2010). Small POC can drive vertical POC fluxes across the mesopelagic layer during episodes of convection (Bishop
et al., 1986; Dall’Olmo and Mork, 2014; Lacour et al., 2019) or subduction (Llort et al., 2018; Omand et al., 2015;
Resplandy et al., 2019), potentially making large contributions to POC export (Alonso-Gonzalez et al., 2010; Henson et al.,
2015). Sources of sPOC to the mesopelagic layer and below it are not limited to gravitational sinking or detrainment from
the surface, because sPOC can be produced through the fragmentation of sinking bPOC, caused by physical disaggregation,
75 bacterial solubilization and zooplankton activity (Briggs et al., 2020; Goldthwait et al., 2004; Mayor et al., 2020; Stemmann
et al., 2004b), and also through bacterial chemosynthesis (Arístegui et al., 2009). Altogether, these findings illustrate how
our limited knowledge of POC characteristics and cycling hampers mechanistic understanding of the BCP and mesopelagic
carbon budgets (Burd et al., 2010; Giering et al., 2014; Steinberg et al., 2008).

80 Biogeochemical models designed to capture only gravitational POC sinking fail to represent POC stocks in the ocean
interior. Aumont et al. (2017) recently showed that the Pelagic Interactions Scheme for Carbon and Ecosystem Studies
model (PISCESv2; Aumont et al., 2015) underestimated POC by one order-of-magnitude or more below the epipelagic
layer. This pitfall is likely common to any state-of-the-art model with similar structure (Laufkötter et al., 2016; Sférian et
al., 2020). Aumont’s work also showed that the implementation of a variable reactivity scheme for POC improved
85 dramatically the fit to observed deep-ocean POC concentrations, without harming vertical POC flux estimation. This
parameterization treats detrital particles, both small and big, as a mixture of particles distributed along a reactivity continuum
(RC). The most labile fractions are rapidly consumed below the productive illuminated surface layer, such that vertically
exported POC becomes progressively more refractory. This results in enhanced preservation of sPOC in the model and a
much more realistic fraction of sPOC with respect to total POC (tPOC) in the ocean interior.

90 Despite this breakthrough in the representation of POC fractions in PISCESv2_RC (hereafter “PISCES”), the new
parameterization was evaluated using only sparse in-situ measurements. During the last decade, the launching of the
biogeochemical Argo (BGC-Argo) program of robotic observations has revolutionized the study of particles in the ocean



interior (Claustre et al., 2020). BGC-Argo floats provide vertical profiles of temperature, salinity, bio-optics and chemical
95 variables between 0–1000 m every 1 to 10 days in near-real time, and are thus especially well suited to study particles in the
mesopelagic layer, where the strongest POC gradient occurs. The rapidly growing fleet of BGC-Argo floats equipped with
bio-optical sensors enables comparison between models and observations at global scales with enhanced spatiotemporal
resolution. Unfortunately, BGC-Argo floats measure only a bio-optical proxy of POC, the particulate backscattering
coefficient (usually at 700 nm, b_{bp700}) and empirical conversion factors are needed to estimate POC from b_{bp700} (Cetinić et al.,
100 2012; Stramski et al., 2008).

In this study we compare sPOC and bPOC concentrations estimated from BGC-Argo floats to their PISCES-simulated
counterparts, as well as satellite-retrieved surface POC. The comparison is enabled by a novel empirical algorithm to convert
 b_{bp700} to POC. Observations and simulations are matched in 3D (biome-wide climatological scale) and 1D (at defined
105 locations over an annual cycle). These complementary strategies allow us to evaluate the skill of PISCES at simulating POC
stocks and fractions, and indirectly the drivers of POC export and mesopelagic POC budgets, in globally representative
biomes.

2 Methods

2.1 Definition of vertical and horizontal domains

110 Studies of the BCP usually decompose the ocean into vertical domains: a surface layer where autotrophic activities
dominate, and one or several ocean interior layers where heterotrophic processes dominate. Functional definitions based on
light penetration, peak export production, vertical mixing or long-term carbon sequestration are usually the most appropriate
ones for process studies (Buesseler and Boyd, 2009; Buesseler et al., 2020; Guidi et al., 2015; Palevsky and Doney, 2018).
Because this paper is mainly descriptive and combines observations and simulations, we will refer to layers defined by fixed
115 depths: epipelagic (0–200 m), mesopelagic (200–1000 m) and bathypelagic (1000–4000 m).

Over the horizontal dimensions, our comparisons between observations and model results rely on the ocean biomes defined
by Fay and McKinley (2014). These authors subdivided each ocean basin (Atlantic, Pacific, Indian, and Southern Ocean)
into different biomes on the basis of observed variables, namely: sea surface temperature, spring/summer chlorophyll *a*
120 concentrations (Chl_a), ice fraction, and maximum mixed layer depth (MLD), all on a $1^\circ \times 1^\circ$ grid. This division resulted in 17
regions ascribed to one of the following five biomes: the ice biome, the subpolar seasonally stratified biome, the subtropical
seasonally stratified biome, the subtropical permanently stratified biome, and the equatorial biome. The analyses reported
herein focus on the following four biomes (Fig. 1): the seasonally stratified North Atlantic subpolar gyre (NASPG); the
permanently stratified Atlantic and Pacific subtropical gyres, which were grouped together (STG); the seasonally stratified
125 Southern Ocean (Subantarctic); and the Mediterranean Sea, which was added here owing to the abundance of BGC-Argo



data, and represents a seasonally stratified subtropical biome. Fay and McKinley's definition allows biome boundaries to change from one year to another. Here we analysed only data from the core of each biome, defined as the grid cells that never changed classification during the 1998–2010 satellite observation periods.

2.2 BGC-Argo observations

130 The global dataset acquired by the array of BGC-Argo floats was downloaded on 14 January 2020 from the Global Data
Assembly Center hosted by Ifremer (<ftp://ftp.ifremer.fr/ifremer/argo/dac/>) (Argo, 2000). We selected floats equipped with at
least a Chla fluorometer and a sensor for optical backscattering at 700 nm (b_{bp700}), in addition to the conductivity-
temperature-depth (CTD) probe. The downloaded measurements had undergone the standard processing, which includes the
application of calibration equations to raw sensor output and the performance of near-real-time quality control to both CTD
135 (Wong et al., 2021) and Chla measurements (Schmechtig et al., 2018). Since no specific quality control procedure has been
established yet for b_{bp700} profiles, the latter were only flagged according to the general criteria (Schmechtig et al., 2016).
Thus, we used all b_{bp700} measurements with quality control flag ≤ 3 (equivalent results were obtained with flag ≤ 2). Two
different processing pipelines were applied to different subsets of the BGC-Argo data, as described below.

2.2.1 Global gridded climatologies (3D approach)

140 The global dataset acquired between 2010 and 2019 was used to produce global gridded monthly and seasonal climatologies
for b_{bp700} and Chla. The measurements were binned onto the ORCA2_L31 grid used for NEMO-PISCES simulations (see
2.4.1), which has an horizontal resolution of about 2° that increases to 0.5° in the meridional direction in the equatorial
domain, and 30 oceanic vertical levels between the surface and the ocean bottom. The thickness of the vertical bins increases
progressively from 10 m at the surface to 339 m in the 22nd bin (870–1209 m), the deepest one containing BGC-Argo data.
145 In each grid element, the average, median, range and data counts were computed. Profiles from the CSIRO and INCOIS data
assembly centers were not used because, at the time of download, they had not taken into consideration the new calibration
files provided by the manufacturer. A total of 72460 profiles were used to calculate the global gridded climatologies.

2.2.2 Profile time series for individual floats sampling at higher resolution (1D approach)

A subset of the floats, deployed mostly by the projects NAOS, remOcean and Bio-Argo France (model NKE PROVOR
150 CTS-4), were programmed to sample at higher temporal and vertical resolution than the Argo defaults (10 days and 10 m).
These floats made vertical profiles between 1,000 m and the surface every 2, 5 or 10 days with a vertical resolution of 10 m
between 1,000 and 250 (or 350) m, 1 m between 250 (or 350) and 10 m, and 0.2 m between 10 m and the sea surface. We
processed this dataset with a dedicated pipeline to extract additional information on POC size fractions and their dynamics.
Along each vertical profile we computed depth, conservative temperature, absolute salinity, σ_θ and spiciness (Flament, 2002)
155 from the calibrated pressure, temperature and salinity using the R package *oce* (Kelley, 2011). The MLD was calculated as
the shallowest depth where σ_θ exceeded the surface reference value by 0.03 kg m^{-3} . The surface reference corresponded to



the σ_θ at 5 m after applying a 5-point running mean to the top 10 m of the profile. Eleven additional MLD criteria were also calculated to assess the robustness of the approach (Fig. S1). Following Briggs et al. (2011, 2020), each b_{bp700} vertical profile was smoothed with sequential 11-point running-minimum and running-maximum filters to separate the baseline from the spikes. The baseline signal corresponds to the bulk population of small particles, whose diameter is smaller than 100 μm and mostly between 0.5 and 30 μm (Dall’Olmo et al., 2009; Organelli et al., 2018). Each spike reflects the passage of a particle (organism or aggregate) larger than about 100 μm in front of the sensor window. Unlike Briggs et al. (2020), we did not subtract from the baseline profile the 850–900 m signal, which in that study was attributed to a background of small refractory particles with constant concentration. The baseline and spike signals were converted to sPOC and bPOC, respectively, as described in the next section. All measurements were subsequently averaged into 18 vertical bins of progressively increasing thickness, such that the deepest bins contained at least 10 measurements. Finally, each profile was interpolated onto the L75 vertical grid commonly used in NEMO simulations. This grid has 46 bins between the surface (0–1 m) and the deepest layer considered here (901–996 m). The profile time series was temporally binned into 5-day periods.

For the comparison to PISCES 1D simulations, BGC-Argo time series were cut into one-year periods (shifted by 6 months in the Southern hemisphere), which we will call coherent annual time series (CATS) hereafter. The CATS fulfilled the following conditions: (1) sampling dates spanned at least between days of year 25 and 340; (2) the float remained in the same region and did not cross major oceanic fronts according to the vertical-temporal evolution of temperature, salinity, σ_θ and spiciness; (3) bottom depth was > 1000 m for all profiles (bathymetry obtained from the 15 arc-second GEBCO 2019 product; https://www.gebco.net/data_and_products/gridded_bathymetry_data/gebco_2019/gebco_2019_info.html); and (iv) the Chla and b_{bp700} sensors were stable according to both the vertical profiles and the continuous measurements acquired during drift at 1000 m between profiles. A total of 50 CATS from 28 different floats were selected, with 10–16 CATS in each biome, 32 (18) in the Northern (Southern) hemisphere (Table S1).

2.3 Conversion of b_{bp700} to POC

To convert the profiles of the backscattering coefficient at 700 nm (b_{bp700}) to POC we developed an empirical algorithm, whose behaviour is summarized in Fig. 2, building on previous studies (Bol et al., 2018; Evers-King et al., 2017). The variability of POC/b_{bp700} enclosed in this algorithm results from processes that alter the size distribution, dominant shapes, and chemical composition of the particle assemblage, and ultimately its bulk optical properties, as discussed in section 4.2. Further details are provided in the Appendix. The algorithm estimates the POC/b_{bp700} ratio along the vertical profile between 0 and 1000 m, and proceeds in two steps. First, the POC/b_{bp700} ratio is calculated by prescribing a POC/b_{bp700} ratio in the surface layer ($z_{\text{surf,biome}}$) and an exponential decrease with depth in the underlying water column, which converges asymptotically towards a constant deep value (c):

$$\text{POC}/b_{bp,700}(z) = c + a_{\text{biome}} * \exp(-b * (z - z_{\text{surf,biome}}) * 0.001), \quad z > z_{\text{surf,biome}} \quad (1)$$



190

The a_{biome} coefficient is biome-specific, whereas the asymptote at depth is fixed at $c = 1000 \text{ mmol C m}^{-3} \text{ m}$. The $z_{\text{surf,biome}}$ corresponds to the 5% quantile of the climatological MLD in summer in a given biome. The $\text{POC}/b_{\text{bp},700}$ ratios at $z_{\text{surf,biome}}$, corresponding to $a_{\text{biome}} + c$ in Eq. 1, are taken from the literature and range between 2600 and 4900 $\text{mmol C m}^{-3} \text{ m}$ (Fig. 2; Table A1). Second, the $\text{POC}/b_{\text{bp},700}$ profile derived from Eq. 1 is modified by extrapolating a constant $\text{POC}/b_{\text{bp},700}$ value, taken from a reference depth, z_{ref} , to the sea surface. In each vertical profile, z_{ref} is defined as the deepest of $z_{\text{surf,biome}}$ and the MLD:

195

$$\text{POC}/b_{\text{bp}700}(z) = \text{POC}/b_{\text{bp}700}(z_{\text{ref}}), \quad z \leq z_{\text{ref}}; \quad z_{\text{ref}} = \max(z_{\text{surf,biome}}, \text{MLD}) \quad (2)$$

200

The exponential decrease prescribed by Eq. 1 is similar to that proposed by Bol et al. 2018, except for the inclusion of the constant term c that prevents the ratio from becoming 0 at depth. The slope of the exponential decrease ($b = -6.57$) is constant in all biomes and based on our fit to the Cetinić et al. (2012) dataset, using the same depth bins as Bol et al. (2018), but additionally forcing the curve towards c at 1000 m.

205

The uncertainty of regional $b_{\text{bp}700}$ -POC conversion factors in the epipelagic is typically $<10\%$ according to the standard error of the POC vs. $b_{\text{bp}700}$ linear regression slopes (Table A1). The few available measurements in the mesopelagic suggest a $\text{POC}/b_{\text{bp}700}$ uncertainty lower than a factor of two. Through this study, we will assume that model/observation ratios larger/smaller than 2/0.5 can safely be regarded as model over/underestimates, which possibly is a conservative criterion for the epipelagic layer.

210

The conversion of $b_{\text{bp}700}$ to POC was done using different MLD data for the global climatologies and the CATS. For the global climatologies we used the Monthly Isopycnal & Mixed-layer Ocean Climatology (MIMOC) of Schmidtko et al. (2013), downloaded from <https://www.pmel.noaa.gov/mimoc/>, which was reprojected onto the ORCA2 horizontal grid. Although MIMOC is based on an algorithm that evaluates several MLD criteria, it has been shown to be globally consistent with the MLD based on a $0.03 \text{ kg m}^{-3} \sigma_\theta$ threshold (Holte and Talley, 2009; Sallée et al., 2021). For the float time series, we used the MLD defined by a 0.03 kg m^{-3} threshold computed for each individual profile.

215

2.4 Ocean color satellite data

Satellite observations for the 1997–2019 period were downloaded from GlobColour (<https://www.globcolour.info>), a merged multisensor dataset, on 2 March 2020. Monthly sea-surface POC fields based on the algorithm of Stramski et al. (2008) were used to compute monthly climatologies that were subsequently reprojected onto the ORCA2 grid.

220



2.5 PISCES simulations and matching with observations

Simulations were run using the ocean biogeochemistry model PISCESv2 (Aumont et al., 2015) with the RC parameterization for detrital POC (Aumont et al., 2017). The configuration of PISCES used here has 24 tracers: two classes of phytoplankton (“nanophytoplankton” and diatoms), detrital particles (small and big), and zooplankton (micro- and mesozooplankton), plus
225 18 additional tracers that comprise dissolved inorganic macronutrients and iron, inorganic carbon chemistry variables, dissolved organic carbon (DOC), and different particulate stocks of iron and silica. Phytoplankton growth depends on light, inorganic nitrogen, phosphorus and iron, with an additional silicate requirement for diatoms. Microzooplankton and mesozooplankton consume the two classes of phytoplankton and detrital particles with different preferences, and mesozooplankton also predate on microzooplankton. Detrital particles are produced through the mortality of phytoplankton
230 and zooplankton (which are routed to small and big particles in different proportions), zooplankton sloppy feeding, and DOC coagulation. Production of large detritus also results from enhanced diatom mortality upon bloom collapse, aggregation of small detritus, and zooplankton mortality and fecal pellet production (the latter two derived from a closure term that accounts for unresolved higher trophic levels). Small and big detrital particles are nominally smaller/larger than 100 μm and sink, respectively, at 2 and 50 m d^{-1} . Both small and big detritus are remineralized by implicit bacterial activity, and consumed by
235 flux-feeding mesozooplankton. Remineralization follows first-order kinetics with an initial specific rate “k” of 0.035 d^{-1} (at 0°C) for freshly produced detritus in the upper mixed layer. This “k” decreases with depth as an emergent result of the RC parameterization. The flux feeding rate depends on the particles’ sinking flux, and thus attenuates the flux of large particles more strongly. Additionally, a small fraction of the large detritus intercepted by flux feeders is fragmented into small detritus. Phytoplankton growth rates and remineralization rates increase with temperature with a Q_{10} of 1.9, whereas
240 zooplankton growth rates have a Q_{10} of 2.14.

To evaluate PISCES simulations against in situ POC measurements or their proxies, the correspondence between PISCES tracers (*in italics*) and observed POC fractions has to be established. In this study we assumed that sPOC corresponds to the sum of PISCES-simulated nanophytoplankton (*PHY*), diatoms (*PHY2*), small detrital particles (*POC*) and microzooplankton
245 (*ZOO*), whereas bPOC corresponds to the sum of PISCES-simulated big detrital particles (*GOC*) and mesozooplankton (*ZOO2*) (Table 1). Total POC (tPOC) corresponds to the sum of those six PISCES tracers or, what is the same, sPOC + bPOC. Heterotrophic prokaryotes (*BACT*) are not a prognostic tracer in PISCES, and are not explicitly included in our analysis. The correspondence between observed and simulated POC fractions, explicit and implicit, is discussed in section 4.3.

250 2.5.1 PISCES 3D simulations vs. biome-aggregated observations

For the global-scale comparison between PISCES outputs and observations from BGC-Argo and satellites, we used the simulation presented by Aumont et al. (2017), which was forced by pre-computed dynamical fields from a pre-industrial run



of the ocean circulation model NEMO. Global monthly climatological fields of the PISCES tracers were used to compute seasonal climatologies of modeled sPOC, bPOC and tPOC. To enable direct comparison to the BGC-Argo observations, model output was resampled at locations where BGC-Argo profiles were available over the 2010–2019 period. Prior to comparison with modeled fields, BGC-Argo observations were further screened to remove “outliers” in each biome and season. Outliers were defined as grid cells where the mean b_{bp700} in the upper 50 m was above the 95% percentile or greater than 0.008 m^{-1} (Briggs et al., 2020). The same resampling was applied to satellite-retrieved POC.

2.5.2 PISCES 1D simulations vs. BGC-Argo coherent annual time series (CATS)

A more detailed comparison was undertaken by matching each of the CATS from individual BGC-Argo floats with a PISCES water-column (“PISCES 1D”) simulation. The match was based on the coherence between the seasonal cycle of MLD observed by the float and the turbulent layer simulated by NEMO. The pre-computed dynamical fields used to evaluate the match-ups were obtained from an ocean-only historical simulation (NEMO v3.6) at 1-degree resolution with 75 vertical levels (ORCA1_L75 grid) forced with the JRA-55 atmospheric reanalysis that covered the 1958–2018 period (Tsuji no et al., 2020) following the OMIP2 protocol (Griffies et al., 2016). The float-observed MLD and the NEMO-simulated turbocline depth (defined by turbulent diffusivity $> 5 \cdot 10^{-4} \text{ m}^2 \text{ s}^{-1}$) were compared over the entire annual cycle in all the model grid cells that had been visited by the float on a given year. The best model grid cell was selected on the basis of model-observations correlation, root-mean-square error, and time lag in the onset date of summer stratification. An example of the metrics used to match NEMO dynamical fields and BGC-Argo MLD is provided in Fig. S1-S4.

PISCES 1D offline simulations were forced using the dynamical fields from the selected model grid cells. The same annual forcing, corresponding to the year of the BGC-Argo observations, was repeated over 5 simulation years. After 4 years of spin-up, the output from year 5 at 5-days resolution was used for the comparison to the BGC-Argo CATS. Initial conditions (climatological fields of inorganic nutrients and carbon chemistry variables) and boundary conditions (atmospheric deposition) were the same used for PISCES 3D (Aumont et al., 2015, 2017). Nutrient fields were restored towards the mean annual profile below 300 m. This procedure avoided drift in nutrient stocks by replenishing the upper ocean with the same amount of nutrients each year, resulting in regular seasonal cycles after one year and identical cycles from year 4 onwards.

3 Results

3.1 Climatological POC fields

This section describes the comparison among tPOC fields estimated from BGC-Argo and satellite observations and PISCES simulations across four ocean biomes. Fig. 3 compares monthly climatologies at the sea surface (0–20 m), Fig. 4 compares seasonal climatologies between 0–1000 m, and Fig. 5 displays skill metrics (Pearson’s correlation, model/observations ratio and bias) for the vertical profiles shown in Fig. 4, as well as for the 1D simulations matched to BGC-Argo CATS.



3.1.1 Seasonally stratified subpolar biomes

285 In the subpolar biomes, near-surface tPOC ranged between $\sim 1 \text{ mmol m}^{-3}$ in the winter months and around 5 (Subantarctic) or
10 (NASPG) mmol m^{-3} in early summer. In these biomes, PISCES-simulated tPOC was within the 2.5–97.5% bounds of
BGC-Argo observations for the majority of months (Fig. 3). During the apex of the bloom (months 5–7), however, median
PISCES estimates exceeded those obtained from BGC-Argo (by $\sim 80\%$) and satellites (by $\sim 15\%$). In the Subantarctic, this
290 pattern extended through the fall. Satellite tPOC was in poor agreement with both PISCES and BGC-Argo tPOC outside the
apex of the bloom, as discussed in section 4.1.

PISCES reproduced the vertical decrease of tPOC concentration down to 1000 m (Fig. 4) with generally good skill (Fig. 5),
but some misfits were observed. In the North Atlantic subpolar gyre (NASPG), PISCES underestimated tPOC through the
epipelagic and the upper mesopelagic during the winter by $\sim 40\%$ (Fig. 4) as a result of too vigorous convection in the
295 NEMO dynamical fields that kept phytoplankton under insufficient light exposure. In the Subantarctic biome, simulated
tPOC exceeded BGC-Argo estimates in the upper portion of the mesopelagic layer in spring, and the overestimation pattern
propagated downwards through the summer and fall. A similar but smaller overestimation pattern was observed in the
NASPG in summer and fall.

3.1.2 Permanently and seasonally stratified subtropical biomes

300 In the oligotrophic biomes, monthly median surface tPOC displayed low seasonal amplitude. Total POC concentrations
estimated from BGC-Argo data typically oscillated around 2 mmol m^{-3} , with a maximum/minimum ratio of around 1.6 in the
Mediterranean and 1.3 in the Atlantic and Pacific subtropical gyres (STG). In the STG, satellite and BGC-Argo tPOC were
in good agreement, which could be expected because b_{bp700} -POC conversion factors and satellite POC are based on the same
study (Stramski et al., 2008). On the contrary, PISCES tPOC exceeded BGC-Argo tPOC by around twofold in the STG. In
305 the Mediterranean, satellite tPOC exceeded BGC-Argo tPOC by $\sim 80\%$, pointing to the differences in the respective POC
estimation algorithms. PISCES tPOC was nearly fourfold higher than BGC-Argo tPOC at the surface in the Mediterranean,
an overestimation that results from unrealistic physics in that basin caused by the coarse (2°) model grid (see 3.3 and 4.3).
Vertical tPOC profiles evidenced the shortcomings of PISCES simulations in the oligotrophic gyres. Compared to BGC-
Argo profiles, PISCES simulations produced too-sharp deep POC maxima and underestimated tPOC in the waters above and
310 below (Fig. 4). Overall, these patterns prompted us to examine in greater detail the seasonal cycles of POC in different
biomes.

3.2 Coherent annual time series of sPOC and bPOC: case studies

In this section we describe two CATS from BGC-Argo floats and their PISCES 1D counterparts (section 3.2.1). The floats,
identified by their World Meteorological Organization (WMO) number, are the 6901486 in the NASPG (year 2015) and the



315 6901660 in the South Pacific STG (year 2017). The float 6901486 represents the most productive conditions of our dataset, with annual median (maximum) Chla of 0.60 (10.7) mg m^{-3} and tPOC of 5.5 (16.7) mmol m^{-3} in the near-surface layer (0–20 m). By contrast, float 6901660 represents the most oligotrophic waters, with annual median (maximum) Chla of 0.011 (0.036) mg m^{-3} and tPOC of 1.8 (2.5) mmol m^{-3} in the near-surface layer. In Fig. S5–S10 we provide additional examples of the CATS-PISCES 1D match-ups in the four biomes and in two subregions within the NASPG.

320 3.2.1 Labrador Sea (North Atlantic subpolar gyre)

Float 6901486 was deployed in June 2013 close to the Reykjanes Ridge in the Irminger Sea, NW Atlantic subpolar gyre. After drifting SW carried by the East Greenland Current, the float was trapped in the Labrador Sea cyclonic circulation between 2014 and July 2017, when it stopped communication after completing 344 profiles (cycles). During its multi-year sampling in the Labrador Sea (56–60°N latitude and 48–54°W longitude), over a bottom depth of around 3500 m, the float
325 showed stable physical and bio-optical records at 1000 m, broken only by winter convection events, and recurring annual patterns of spring-summer phytoplankton blooming and vertical carbon export as depicted by Chla and POC profiles. Here we describe the year 2015 (Fig. 6), characterized by deep convection during February and March, when the MLD generally exceeded 1000 m (Fig. S1). Epipelagic tPOC increased rapidly upon water-column re-stratification in mid-April and peaked in mid-May. A secondary bloom peaked in late June after a transient MLD deepening caused by stormy weather. Epipelagic
330 tPOC decreased progressively thereafter until a small bloom was observed in October linked to pycnocline erosion. This bloom terminated rapidly and epipelagic tPOC reached the baseline level in late December. The sPOC fraction dominated epipelagic tPOC all year round, and highest bPOC fractions of nearly 20% were recorded at the apex of the spring-summer blooms. Distinct vertical particle export events were observed in May and June, matching the surface phytoplankton blooms, and August, when nutrient limitation likely triggered bloom collapse. These export pulses produced synchronous increases in
335 sPOC and bPOC through the mesopelagic layer, though with different magnitudes. After reaching relative minima in October, mesopelagic sPOC and tPOC increased again in November, but they showed different vertical patterns.

The matching PISCES 1D simulation captured with good skill the patterns of sPOC and bPOC in the epipelagic and, to a lesser extent, the mesopelagic layer (Fig. 6). Excellent correlation ($r = 0.92$) and bias (-0.5%) between BGC-Argo and
340 PISCES were found for vertically integrated epipelagic tPOC (Fig. 6i). A delayed start of the bloom was observed in the simulation, which can be partly attributed to a delay of around one week in the onset of permanent stratification in the model. It is also plausible that modelled phytoplankton reacted too weakly to the cessation of deep convection, which was captured by alternative MLD metrics in BGC-Argo profiles (Fig. 6a and b). Despite the general good agreement between observed and simulated sPOC, the model produced a conspicuous plume of sPOC that sank from the surface spring bloom
345 into the mesopelagic layer, at the prescribed constant rate of 2 m d^{-1} , which was not found in the observations. In the core of this plume, PISCES POC exceeded BGC-Argo sPOC by more than twofold. A similar model-observations mismatch was observed in all the northern and southern subpolar CATS as well as in some CATS in the Mediterranean (Figures S5-S8 and



S10). On average, simulated bPOC exceeded BGC-Argo bPOC by 36% and 96% in the epi- and mesopelagic layers, respectively. The largest overestimation was observed during the midsummer export event. On the other hand, bPOC
350 underestimation was found during the May bloom between 0–400 m.

PISCES qualitatively reproduced the late summer peak of mesopelagic bPOC, which was observed in all the subpolar North Atlantic CATS. On the contrary, it failed to reproduce both the decrease of sPOC and bPOC in fall between 600–800m and the bPOC increase below 800 m. The latter occurred in 6 out of 11 CATS in the NASPG, all located in the Labrador Sea.
355 The apparent decoupling of deep mesopelagic bPOC from the overlying water column may be related to the insufficient temporal resolution of BGC-Argo profiling during that period compared to bPOC sinking speed, or reflect bPOC export events from surface waters areas not located vertically over the float (Siegel and Deuser, 1997).

3.2.2 South Pacific subtropical gyre

Float 6901660 was deployed in March 2015 in the western South Pacific STG, and drifted westwards until it deflected SW
360 while approaching Tahiti. As of March 2021, the float was still active and had completed 244 cycles with stable continuous records at the 1000 m drift depth. Between July 2017 and June 2018 (18–21°S latitude and 148–157°E longitude), the period selected for the CATS analysis, the BGC-Argo profiles portrayed a stably stratified water column typical of the core of the subtropical gyres (Fig. 7). Vertical mixing events that reached a depth of around 100 m were observed in July, August and October. However, their effect on surface sPOC was hardly noticeable, indicating that turbulent entrainment of nutrients was
365 too weak to stimulate new production significantly. A deep Chla maximum was present all year round between 150 and 200 m as identified by the maximum Chla gradient. This Chla maximum did not translate into a deep POC maximum. The fraction bPOC/tPOC was consistently around 6% in the epipelagic and 12% in the mesopelagic according to the vertically integrated stocks. The vertical-temporal distribution of bPOC was patchy in the lower mesopelagic (500–1000 m), perhaps reflecting the difficulty to detect rare aggregates from b_{bp700} spikes.

370 The epipelagic tPOC stock (driven by sPOC) simulated by PISCES matched well the observations, with a high temporal correlation coefficient ($r = 0.69$; Fig. 7i) despite the low seasonal variability in this tropical setting. The low mean bias of epipelagic sPOC (9%) resulted from mutually compensating biases, as PISCES overestimated sPOC between the base of the mixed layer and the deep Chla maximum, and underestimated sPOC below it. In the mesopelagic layer, vertically integrated
375 PISCES sPOC was on average 45% lower than BGC-Argo sPOC, and showed low negative temporal correlation to the observations. Regarding bPOC, the simulated stock was nearly twice as large as BGC-Argo estimates in the epipelagic, with the largest overestimation seen in the deep Chla maximum. In the mesopelagic, PISCES bPOC exceeded BGC-Argo estimates by 25% on average. Despite model-observations discrepancies in terms of bPOC concentration, PISCES simulations supported the increase in the bPOC/tPOC fraction between the epipelagic and the mesopelagic layers.



380 3.3 Coherent annual time series of sPOC and bPOC: generalized approach

Although each of the 50 CATS included in this study has unique features, some of the misfit patterns between PISCES and BGC-Argo data described in the previous section are common to the majority of CATS in a given biome or, more broadly, in subpolar vs. subtropical biomes. In this section we generalize the quantitative comparison between the 50 BGC-Argo CATS and their PISCES 1D counterparts across the four biomes. We consider separately the epipelagic and mesopelagic domains, focusing on mean annual sPOC and bPOC standing stocks (Fig. 8), the sPOC/tPOC fraction (Fig. 9), and the mesopelagic Teff of sPOC and bPOC (Fig. 10).

Epipelagic sPOC stocks ranged between 193–425 mmol C m⁻² and 282–537 mmol C m⁻², respectively, according to BGC-Argo observations and PISCES 1D simulations. Although the ranges of the different biomes overlapped, smaller stocks were usually found in the more oligotrophic (STG and Mediterranean) biomes. The agreement between simulated and observed epipelagic sPOC was better in the STG and NASPG biomes, whereas simulated epipelagic sPOC exceeded observations by around 50% in the Mediterranean and Subantarctic biomes. Still, a significantly positive correlation between simulated and observed stocks ($r = 0.45$, $p = 9 \cdot 10^{-4}$) was found overall.

In the mesopelagic domain, observed and simulated sPOC stocks ranged between 145–283 mmol C m⁻² and 105–308 mmol C m⁻², respectively, and the correlation between simulated and observed mesopelagic sPOC stocks was not significant ($r = -0.08$, $p = 0.55$). PISCES sPOC was similar to or slightly higher than BGC-Argo sPOC in the subpolar biomes, but up to two-fold lower in the STG and Mediterranean biomes (as already shown in Fig. 4 and 7).

Epipelagic bPOC stocks were smaller and showed wider inter-biome variability than sPOC stocks, with around twofold higher bPOC in subpolar biomes. The positive correlation between simulated and observed bPOC was highly significant ($r = 0.78$, $p = 2 \cdot 10^{-11}$). Yet, PISCES bPOC (range 19–83 mmol C m⁻²) typically exceeded BGC-Argo bPOC (range 27–119 mmol C m⁻²) by around 50%, and up to threefold for some CATS. A lower but still highly significant correlation was found in the mesopelagic ($r = 0.64$, $p = 5 \cdot 10^{-7}$), where PISCES bPOC was usually within a factor of 1.5 of observations, except for the NASPG biome where it exceeded BGC-Argo bPOC by around twofold.

The sPOC/tPOC fraction showed low variability in the epipelagic layer (Fig. 9), with a median (range) of 89% (84–94%) and 85% (75–91%) for BGC-Argo and PISCES, respectively. The simulated sPOC/tPOC fraction was within $\pm 10\%$ of BGC-Argo estimates for all biomes except the NASPG, where PISCES tended to underestimate the observed percentage of sPOC. A significant positive correlation ($r = 0.56$, $p = 2 \cdot 10^{-5}$) was found between simulations and observations in the epipelagic layer. The sPOC/tPOC fraction was lower in the mesopelagic layer according to both BGC-Argo (75–90%) and PISCES (66–85%) estimates. In this case, CATS from the Subantarctic biome showed excellent model-observations agreement,



whereas PISCES was 20% lower than BGC-Argo estimates in the other three biomes. No significant correlation was found between the simulated and observed sPOC/tPOC fraction in the mesopelagic.

415

Transfer efficiency (Teff; Fig. 10) was computed as the ratio between the sPOC or bPOC concentrations in the depth bins centered at 697 m (range 662–734 m) and 200 m (range 190–210 m). The shallowest bin corresponds to the bottom of the epipelagic layer, and the 500 m interval was chosen following previous studies (Lam et al., 2011; Dall'Olmo and Mork, 2014). Different depth ranges between 180 and 800 m gave similar Teff patterns. Analysis of Teff yielded some important insights:

420

1. Small and big POC showed similar Teff, both in the observations (medians of 0.39–0.41) and in the model (medians of 0.27–0.29). Similar patterns were found when each biome was considered separately.
2. BGC-Argo Teff usually exceeded PISCES Teff and spanned a wider range. The best agreement was generally found in the STG and the Subantarctic biomes, and the poorest agreement occurred in the Mediterranean where BGC-Argo Teff was typically twice the modelled Teff.
3. Distinct patterns were found for four CATS in the Labrador Sea (NASPG) characterized by high epipelagic tPOC ($>440 \text{ mmol C m}^{-2}$). In this subset, PISCES and BGC-Argo Teff were in good agreement for sPOC (median 0.40 for both) whereas, for bPOC, PISCES Teff (0.36–0.45) doubled BGC-Argo Teff (0.12–0.28), which had some of the lowest values of the dataset. These CATS showed a bPOC minimum at 600–800 m in fall, which PISCES could not reproduce (section 3.2.1).
4. PISCES and BGC-Argo Teff showed a weak positive correlation for sPOC ($r = 0.26$, $p = 0.07$), with some improvement when the Labrador Sea “outliers” were removed ($r = 0.34$, $p = 0.02$). A negative correlation between simulations and observations was found in the case of bPOC Teff ($r = -0.29$, $p = 0.04$), which became non-significant without the Labrador Sea “outliers” ($r = 0.04$, $p = 0.81$).

425

430

435

Our observational estimates are sensitive to the choice of b_{bp700} -POC conversion factors. These factors are especially uncertain in the mesopelagic due to data scarcity, which prompted us to use a constant global value for “c” in Eq 1. (Fig. 2); $c = 1000 \text{ mmol C m}^{-2}$ is the asymptotic POC- b_{bp700} conversion factor below 1000 m, taken from Cetinić et al. (2012). To address this uncertainty, we conducted sensitivity tests where c was halved or doubled. The resulting range of 500–2000 mmol C m^{-2} is probably generous, as our indirect estimates based on the study of Bishop et al. (1999) suggest a plausible range of 815–1630 mmol C m^{-2} (Appendix A). As expected, changing c had little effect on epipelagic POC, a larger effect on mesopelagic POC and Teff, and no effect on the sPOC/tPOC fraction (because the same conversion factor is used to estimate sPOC and bPOC). Halving c resulted in steeper POC profiles, which brought mesopelagic sPOC closer to the 1:1 line in the STG and Mediterranean, at the expense of increasing the sPOC bias in the subpolar biomes and that of bPOC everywhere (Fig. S11). Doubling c caused a less steep vertical decrease of BGC-Argo POC, which overall worsened the model-observations agreement in the mesopelagic (Fig. S12) for sPOC stocks, bPOC stocks (except in the NASPG) and Teff.

440

445



4. Discussion

4.1 Towards a globally consistent picture of POC fields in observations and models

Global quantification of POC stocks through the water column has been elusive until recently. On the one hand, direct
450 chemical measurements (Lam et al., 2011) and indirect bio-optical observations from ships (Bishop et al., 1999; Gardner et
al., 2006) were sparse, and the ocean interior was severely undersampled compared to the euphotic layer. On the other hand,
biogeochemical models were unable to capture even the order-of-magnitude POC concentration in the meso- and
bathypelagic layers (Aumont et al., 2017). Our joint analysis of PISCES simulations, satellite observations and over 70,000
BGC-Argo vertical profiles reveals a globally consistent picture across the epi- and mesopelagic layers (Fig. 3-10). PISCES-
455 simulated tPOC concentration is on average within a factor of 1.56 (1.42) of BGC-Argo estimates for the median (mean)
seasonal biome profiles shown in Fig. 4 (Mediterranean excluded). Aumont et al. (2017) reported a similar reliability index
of 1.6 for the comparison between PISCES and in situ chemically determined POC profiles. Thus, our evaluation lends
further confidence to the POC reactivity continuum parameterization implemented in PISCES, which represents both sPOC
and bPOC as a mixture of fractions with different lability (Aumont et al., 2017), in globally representative biomes.

460

PISCES simulates a global tPOC stock of 4 Pg C, shared in a proportion of 39% (1.6 Pg C), 25% (1 Pg C) and 36% (1.4 Pg
C) between the epi-, meso- and bathypelagic layers (Table 2). The PISCES-derived estimate for the epipelagic layer, 1.6 Pg
C, lies well within the range of previous estimates based on satellite observations. Gardner et al. (2006) estimated the global
POC stock within the first attenuation depth using a compilation of in-situ POC and c_p measurements leveraged by ocean
465 color satellite data. They obtained a global stock of 0.43 Pg C, and invoked some scaling arguments to estimate that the total
POC stock down to middle-mesopelagic “background levels” would range 1–2 Pg C. Stramska (2009) obtained a global
epipelagic POC stock of 1.8–2.3 Pg C using the algorithm of Stramski et al. (2008). Our analysis of the match-ups between
BGC-Argo and satellite observations indicates that the latter algorithm overestimates POC at high latitudes outside of the
summer season (Fig. 3). Potential explanations are the satellite algorithm being calibrated mostly against samples from lower
470 latitudes (50°N–30°S), or its sensitivity to the differential atmospheric attenuation of the blue and green wavelengths at low
solar elevation (i.e. at high latitudes in winter). Recently, Evers-King et al. (2017) calculated the global mixed-layer POC
stock using several satellite algorithms (including that of Stramski et al., 2008) and indicated that 0.77–1.3 Pg C was a
plausible range. Our PISCES-based estimate for the mixed-layer POC stock, using the same MLD climatology (Schmidtko
et al., 2013), is 0.58 Pg C. In this case, the lower PISCES-derived estimate may arise from the combination of POC
475 overestimation by some satellite algorithms, discussed above, with PISCES' tendency to underestimate mixed-layer POC in
oligotrophic areas. This negative bias in PISCES is compensated by POC overestimation in deep Chla maxima below the
MLD (Fig. 4 and 7), resulting in good agreement between BGC Argo and PISCES over the entire epipelagic layer in the
STG biome (Fig. 8 and S13). Given the limited coverage of in situ seawater sampling and satellite observations in some



480 regions and seasons (Evers-King et al., 2017), further intercomparison between those observations, BGC-Argo data and models is needed to better constrain epipelagic POC stocks.

485 POC in the lower mesopelagic and below has been traditionally treated as a “background” signal (Bellacicco et al., 2019; Gardner et al., 2006; Loisel and Morel, 1998). This approach is convenient for studies that focus solely on upper-ocean processes because POC concentration decreases exponentially with depth. Yet, our global estimates and several previous studies highlight the need to turn our attention to the large POC stocks (>2 Pg C) that reside in the mesopelagic and below it, whose dynamics are still poorly understood. In line with previous studies (Dall’Omo and Mork, 2014; Poteau et al., 2017), we showed that mesopelagic POC exhibits clear seasonal cycles in productive regions (Fig. 6, S5–S7 and S10), owing to their connection with the upper-ocean through numerous biological and physical processes (Boyd et al., 2019; Briggs et al., 2020). Despite being less reactive on average than upper-ocean POC, meso- and bathypelagic organic particles are microbial hotspots that host key biogeochemical functions, from enzymatic decomposition of macromolecules (Arnosti et al., 2012; Baltar et al., 2010a, 2010b) to aerobic and anaerobic respiration (e.g., Karthäuser et al., 2021) and chemosynthesis (Aristegui et al., 2009; Pachiadaki et al., 2017). Moreover, mesopelagic particles are consumed by upper trophic levels that sustain fisheries (Bode et al., 2021; Woodstock et al., 2021).

495 In situ bio-optical measurements are poised to play a key role in monitoring marine POC stocks in layers that cannot be accessed by remote sensing. For example, Sauzède et al. (2020) illustrated the power of merging BGC-Argo and satellite observations to obtain a dynamic 3D view of particle backscattering. Using a data-driven machine learning approach, they were able to predict the profiles of $\log_{10}b_{bp700}$ measured by two BGC-Argo floats in the NASPG and STG biomes (R^2 of around 0.85 and MAPD of around 12%) from the sole knowledge of physical properties of the water column and surface ocean color (remote sensing reflectance). Their approach was recently extended to provide POC estimates (Sauzède et al., 2021), which can be of great utility for constraining biogeochemical models. Here we took an entirely different approach, based on converting b_{bp700} to POC with a simple empirical algorithm (Fig. 2) and then comparing it to the outputs of the PISCES model. Our PISCES-based estimates obtained a median $R^2 = 0.86$ and MAPD = 38% for 5-day depth-binned $\log_{10}POC$ for 28 globally distributed floats. This good skill is remarkable because neither the empirical POC estimates nor PISCES were tuned to maximize their mutual agreement. Still, our study shows that the comparison of bio-optics-derived POC measurements and PISCES is affected by different types of uncertainty that we analyze in the four sections below.

4.2 Bio-optical underpinnings of POC fields based on BGC-Argo observations

510 Accurate interconversion between bio-optical variables and concentrations is key for constraining ocean particle dynamics and their model representation (Bishop et al., 2004; Gardner et al., 2006). The variability in b_{bp700} -POC conversion factors is shaped by several concurrent processes that alter particle abundance, size distribution, shape, composition, and ultimately



optical properties. Below we discuss the processes that appear to drive, to first order, the variability of the $\text{POC}/b_{\text{bp}700}$ ratios embodied in Eq. 1 and 2 (Fig. 2; Appendix A), and the main strengths and weaknesses of our scheme.

Changes in the trophic status appear as the primary driver $\text{POC}/b_{\text{bp}700}$ variability in the epipelagic layer (Cetinić et al., 2012; Figure A1). Productive waters host greater absolute and relative abundance of diatoms (Uitz et al., 2006) (see also Table 2), which have lower POC per cell volume (Menden-Deuer and Lessard, 2000) and are covered with silica frustules that may scatter light more efficiently than naked cells (Twardowski et al., 2001), altogether resulting in lower POC content per unit $b_{\text{bp}700}$ (Cetinić et al., 2012; Oubelkheir et al., 2005). The proportions of different autotrophic and heterotrophic organisms and detritus are also likely to vary with upper ocean productivity (see 4.3). If the mass-specific backscattering coefficients of these components were better known, their systematic variation patterns could be used to develop a continuous formulation for $\text{POC}/b_{\text{bp}700}$, rather than the regionalized conversion factors used here. However, $\text{POC}/b_{\text{bp}700}$ is influenced by other seawater constituents whose occurrence is less predictable. Foremost, biogenic calcite (e.g. from coccolithophores) and desert dust (Claustre, 2002; Loisel et al., 2011), both of which enhance $b_{\text{bp}700}$. In our data set, we detected a CATS (float WMO 6901647, year 2016) that was strongly affected by coccolith backscattering in the Iceland Basin, an area known for its massive coccolithophore blooms (Moore et al., 2012). This CATS was an obvious outlier in our model-observations scatterplots (Fig. S13), likely because coccolith-enhanced $b_{\text{bp}700}$ resulted in spuriously high observed tPOC, and was therefore removed from the analysis.

The decrease in $\text{POC}/b_{\text{bp}700}$ along the vertical axis (Fig. 2) reflects the increase in the particles' index of refraction, hence the backscattering ratio (Cetinić et al., 2012; Nencioli et al., 2010). This change is likely caused by the remineralization of organic materials (Martin et al., 1987) that leaves a higher mineral fraction (Honjo et al., 2008; Lam et al., 2011), and the increase in the structural complexity of aggregates with depth (Organelli et al., 2018). According to our sensitivity analysis (Fig. S11 and S12), the prescribed exponential decrease of $\text{POC}/b_{\text{bp}700}$ towards a constant $\text{POC}/b_{\text{bp}700}$ ($c = 1000 \text{ mmol C m}^{-2}$) at depths $>1000 \text{ m}$ provides a good compromise globally, given the limited knowledge of mesopelagic $\text{POC}/b_{\text{bp}700}$ and its variability across regions. However, the comparison between simulated and observed mesopelagic sPOC (and thus tPOC) is more favorable in subpolar than in subtropical biomes. In the latter, better model-observations agreement was found when $\text{POC}/b_{\text{bp}700}$ was halved ($c = 500 \text{ mmol C m}^{-2}$). A lower c would also bring the simulated T_{eff} for sPOC and bPOC closer to BGC-Argo estimates. It is tempting to hypothesize that lower latitudes have lower mesopelagic $\text{POC}/b_{\text{bp}700}$ owing to the greater proportion of calcite (Francois et al., 2002; Honjo et al., 2008; Lam et al., 2011, 2015). These hypotheses need further verification.

Finally, the decrease of surface $\text{POC}/b_{\text{bp}700}$ with deeper vertical mixing imposed by Eq. 2 reflects the dilution of surface particle assemblages by entrainment of deeper waters (Lacour et al., 2019) with lower $\text{POC}/b_{\text{bp}700}$ (Bol et al., 2018). Modulation of $\text{POC}/b_{\text{bp}700}$ by vertical mixing improves the agreement between PISCES and BGC-Argo data in regions with



545 wide seasonal MLD amplitude such as the NASPG. Note also that if $\text{POC}/b_{\text{bp}700}$ in the mixed layer was constant, it would
have to decrease abruptly below the mixed layer to meet the low $\text{POC}/b_{\text{bp}700}$ in the mesopelagic. On the other hand, the
behavior prescribed by Eq. 2 may not be appropriate for situations when vertical mixing cannot erode the seasonal
thermocline or pycnocline, because in such cases it will entrain water from the deep Chla maximum, and not mesopelagic
water, to the upper mixed layer.

550

Our $\text{POC}-b_{\text{bp}700}$ conversion algorithm omits several aspects that may have caused further uncertainty. Foremost, it assumes
that sPOC and bPOC have the same $\text{POC}/b_{\text{bp}700}$ ratio, which largely corresponds to that of the more abundant sPOC (Fig. 6–
8). In addition, the in-situ data used to parameterize Eq. 1 and 2 are not free of uncertainty (Cetinić et al., 2012; Lam et al.,
2011; Morán et al., 1999; Organelli et al., 2018; Strubinger Sandoval et al., 2021). While the development of more
555 sophisticated $\text{POC}-b_{\text{bp}700}$ interconversion schemes is desirable, the $\text{POC}-b_{\text{bp}700}$ conversion scheme used here provides POC
estimates that are generally consistent with PISCES (Fig. 8) and with previous assessments (Aumont et al., 2017). Moreover,
this scheme allowed us to identify potential shortcomings of satellite-based assessments (Evers-King et al., 2017; Stramski et
al., 2008). Indeed, bio-optical estimates of POC, and more generally BCP studies, would greatly benefit from the
measurement of mass-specific bio-optical properties of various seawater constituents across different ocean basins and
560 depths.

4.3 Correspondence between observed and simulated POC fractions

An additional source of uncertainty in our analysis is the imperfect match between the PISCES tracers and the observable
POC fractions (Table 1). A positive aspect of our evaluation is the reasonable agreement between the simulated sPOC/tPOC
fraction and the BGC-Argo estimates based on the $b_{\text{bp}700}$ spike signal (Fig. 9). Our estimates converge to a global median
565 value of 85%, with 95% of the data between 69–92%, fully within the range of size-fractionated chemical POC
determination (Aumont et al., 2017 and references therein). Our sPOC/tPOC estimates can also be compared to the
suspended POC estimated with the marine snow catcher during spring in subpolar epipelagic and upper mesopelagic waters
(Baker et al., 2017). The slow-sinking POC measured by the marine snow catcher should not be included in this comparison
because it sinks at around 18 m d^{-1} , a range more typical of particles $> 100 \mu\text{m}$ (Giering et al., 2016). The median 94% of
570 suspended (non-sinking) POC reported by Baker et al. is higher than the 86% (81%) sPOC/tPOC estimated here from BGC-
Argo (PISCES) in the subpolar biome, suggesting further comparison between different approaches is needed. The tendency
of sPOC/tPOC to decrease between the epipelagic and the mesopelagic, found in both PISCES and BGC-Argo data (Fig. 9,
Table 2), was also reported in previous studies (Aumont et al., 2017 and references therein; Organelli et al., 2020), lending
further confidence to our estimates. On the other hand, the simulated partitioning of sPOC and bPOC into different living
575 and detrital compartments is probably less realistic, as discussed in greater detail below.



A problematic aspect in the current representation of sPOC in PISCES is the partitioning between phytoplankton and non-phytoplanktonic (detrital + heterotrophic) POC in the upper ocean. This partitioning is far from being well established, neither from bio-optical observations nor from direct determination. Starting with bio-optical approaches, Oubelkheir et al. (2005) found that detritus accounted for around 60% of POC across a wide range in ocean productivity, and 70–85% of POC was assigned to detritus + heterotrophs. These percentages accord well with those found by Claustre et al. (1999) in the tropical Pacific (their Table 1; see also Organelli et al., 2020). By contrast, Bellacicco et al. (2020) suggested that the non-phytoplanktonic b_{bp700} fraction varies widely, between <10% in the productive NASPG to >80% in subtropical gyres. Given the similar refractive indexes of living cells and organic detritus, hence similar POC/ b_{bp700} , the latter and former estimates are hardly compatible when compared in POC units. Estimates based on direct POC stock determinations across wide productivity gradients are also conflicting. Gasol et al. (1997) found a general increase in the autotrophic/heterotrophic ratio with productivity, with ratios as low as 0.1 at low autotrophic biomass. By contrast, Graff et al. (2015) found that phytoplankton accounted for between 15–85% of POC, with decreasing phytoplankton contributions at lower POC or Chla concentration (their figures 4 and 7), leaving no room for heterotrophs and detritus. Indeed, the two latter studies agree in the wide scatter in large-scale POC partitioning patterns, may further confound in situ bio-optical estimates. The low fraction of detrital POC in PISCES near the sea surface, 15–31% (Fig. 4; Table 2) is at odds with most observations, and suggests too slow transfer of planktonic biomass to detritus and/or too fast detrital POC removal, especially in oligotrophic waters.

PISCES bias may also arise from inappropriate representation of some POC reservoirs, such as heterotrophic prokaryotes (bacteria and archaea, *BACT* in PISCES), which have long been recognized as important contributors to the suspended POC (Morel and Ahn, 1990; Gasol et al., 1997). However, *BACT* are not explicitly modelled in PISCES as prognostic tracers, meaning they are not interacting fully with other tracers. Instead, they are diagnosed in the productive surface layer from zooplankton biomass, based on an old model version that had interactive *BACT*. Below this layer, *BACT* biomass is propagated downwards with a power function based on Aristegui et al. (2009), which resembles a Martin curve (Martin et al., 1987) and is therefore very sensitive to the reference depth (Z_0) (Buesseler et al., 2020). We find two main arguments against the inclusion of PISCES-estimated *BACT* in our POC estimates with the current model configuration. First, the empirical *BACT* estimation in PISCES has not been validated, to our knowledge, and may introduce noise in the comparisons. Second, PISCES-simulated POC already includes heterotrophic prokaryotes, because their biomass was not removed from the in situ POC measurements used to adjust the POC parameters in PISCESv2 (Aumont et al., 2017). In consequence, adding *BACT* to sPOC causes overestimation of mesopelagic POC (Fig. S14–S16) and can produce unrealistic temporal patterns (Fig. S15). Nevertheless, we believe that inclusion of prognostic bacteria would enable more realistic simulation of POC stocks, with the potential side effect of improving the simulation of element fluxes in PISCES.

The comparison between simulated and observed bPOC is a novel contribution of our study. The method of Briggs et al. (2011, 2020), originally developed to study intense POC export events, was here extended to estimate sPOC and bPOC



separately over the full annual cycle through the epi- and mesopelagic domains. Our analysis shows that, despite the mismatch in terms of concentration, the bPOC derived from the spikes of high-resolution bio-optical profiles is strongly correlated to the PISCES-simulated bPOC ($r = 0.78$, $r^2 = 0.61$) along a wide trophic gradient (Fig. 8). This result is encouraging and supports the more widespread deployment of instruments that perform high-resolution bio-optical sampling to shed light on the spatiotemporal dynamics of large aggregates and particles (Briggs et al., 2020; Lampitt et al., 1993; Stemmann et al., 2008). On the other hand, it is unclear to what extent the bPOC inferred from the b_{bp700} spike signal is capturing mesozooplankton biomass, in addition to aggregates. Exclusion of PISCES mesozooplankton (*ZOO2*) from the comparison increases model-observations mismatch, with BGC-Argo bPOC exceeding PISCES estimates by around twofold, although the correlation remains nearly unchanged ($r = 0.76$, $p < 10^{-10}$). Imaging devices mounted on BGC-Argo floats may provide more accurate quantification of bPOC, allowing for the separation of detrital bPOC (Trudnowska et al., 2021) from mesozooplankton and micronekton (Haëntjens et al., 2020).

4.4 Importance of realistic physics and model evaluation across scales

In Fig. 5, PISCES simulations and BGC-Argo observations are compared using an array of skill metrics computed on the seasonal vertical profiles of tPOC between 0–1000 m. Starting with the 3D seasonal climatology, we observed that the correlation between the median (aggregated) profiles was generally better than the correlation between the spatially collocated (non-aggregated) profiles within a given biome and season (Fig. 5a), whereas no differences were found in terms of dispersion metrics (Fig. 5b and c). The difference in correlation was larger in subpolar biomes, suggesting that the model-observations spatial mismatch was magnified in regions with more energetic ocean dynamics and sharper physical and biogeochemical gradients, whose real-world location may not be well reproduced by the ocean circulation model used to force PISCES. For PISCES 1D simulations, their correlation coefficients with their CATS counterparts was usually in the high range of the correlation coefficients obtained by the biome-median PISCES 3D profiles. In terms of dispersion metrics, the ensemble of PISCES 1D simulations showed wider dispersion, but the best 1D simulations clearly outperformed the 3D simulation in a given region and season. The better skill of 1D simulations was more evident during spring, a season characterized by the onset of stable stratification after deep winter vertical mixing in middle and high latitudes. The greatest difference between 3D and 1D simulations was found in the Mediterranean, highlighting the more realistic vertical mixing and upper ocean productivity in the 1D simulations.

Our cross-scale evaluation indicates how crucial it is to evaluate model physics before extracting conclusions on biogeochemical model performance (Doney et al., 2004; Kriest et al., 2020; Löptien and Dietze, 2019). In our 1D CATS approach, the skill of PISCES simulations was maximized by carefully matching observed and modelled vertical mixing (Fig. S1–S4), which is a key driver of upper ocean ecosystems. This approach has a subjective component, and may also suffer from the idealized assumption that BGC-Argo profiles reflect mostly vertical-scale processes, disregarding horizontal advection (Alonso-González et al., 2009). Yet, the similar misfit patterns encountered for different CATS within a given



645 biome support the robustness of the 1D matching approach (compare Fig. 6 versus S6, and Fig. 7 versus S9). To further
evaluate this issue, we matched different neighboring NEMO grid cells to the same in situ CATS. Again, this exercise
indicated that our main conclusions are not sensitive to the choices made for 1D model-observations matching (compare Fig.
6 and Fig. S5). Indeed, alternative matching approaches can be devised, each of which with advantages and pitfalls, for
example: (1) sampling the outputs of biogeochemical models at the locations visited by BGC-Argo floats, which may require
high resolution models; (2) deploying virtual BGC-Argo floats (van Sebille et al., 2018) and comparing them statistically to
650 observations; or (3) forcing 1D biogeochemical simulations with observed physical fields, e.g. vertical mixing (Llort et al.,
2015) or light (Terzić et al., 2019). As a general rule, the good skill of the best PISCES 1D simulations (Fig. 5) indicates that
our CATS approach can be used to tease apart model-observations misfits caused by model physics from those caused by the
parametric uncertainty and the structure of the biogeochemical model, opening up new avenues for parameter optimization
(Falls et al., *submitted*) and model development.

655

Our cross-scale evaluation is also informative as to the spatiotemporal scales that can be addressed with a given model setup.
This matter was recently tackled by Bisson et al. (2019) using the export production model of Siegel et al. (2014), which is
forced by satellite-derived primary production. In particular, they showed that this diagnostic model could be optimized to
reproduce global climatological patterns, but exhibited poor skill when faced with non-climatological datasets, which reflect
660 local snapshots of ecosystem functioning. Model evaluation at climatological scales provides an incomplete picture,
especially in productive regions where much POC export can take place during intense but short-lived events (Briggs et al.,
2020). Such events are smoothed out when climatologies are computed, and their coherence with the physical forcing is lost.
Our work shows that a prognostic model like PISCES can afford both event-scale and climatological scale predictions. This
capability is important to test our process-level understanding, which underpins climate change projections.

665 **4.5 Joint use of BGC-Argo and models for process-level understanding**

Properly representing POC stocks is crucial for constraining epi- and mesopelagic carbon budgets and, ultimately, estimating
the strength of the BCP and predicting its future evolution. The mismatch patterns between simulated and observed POC
profiles (Fig. 4, 6 and 7) indicate different types of model shortcomings in subpolar and subtropical latitudes. The poorest
agreement between PISCES and BGC-Argo data is found when their respective estimates of mesopelagic T_{eff} are compared
670 (Fig. 10), which should prompt further research on this key descriptor of the BCP, both in terms of POC fluxes (Buesseler et
al., 2020) and stocks (Lam et al., 2011; this study), and their relationship with the structure and productivity of the upper
ocean ecosystem.

In the subpolar biomes, we find discrepancies between the patterns of sPOC and bPOC vertical export triggered by the
675 intense surface phytoplankton blooms typical of these waters (Fig. 6, S5–S7 and S10). The observed rapid sPOC increase at
depth cannot be explained by the sPOC gravitational sinking, and fragmentation of rapidly sinking bPOC has to be invoked



(Briggs et al., 2020). This fragmentation is most likely caused by zooplankton feeding (Mayor et al., 2020; Stemmann et al., 2004a, 2004b; Stukel et al., 2019) and swimming (Goldthwait et al., 2004), combined with bacterial hydrolysis of aggregate-binding polymers (Arnosti et al., 2012; Baltar et al., 2010a). In relative terms, mesopelagic sPOC increases less strongly than
680 bPOC during blooms (Fig. 6i), which is consistent with sPOC being a byproduct of the transformation of less-abundant bPOC. Fragmentation processes may supply fresher sPOC to the mesopelagic, enhancing the coexistence of suspended particles with variable freshness (Alonso-Gonzalez et al., 2010; Aumont et al., 2017) and overall contributing to POC remineralization (Giering et al., 2014; Mayor et al., 2020).

685 In the subtropical gyres and the most oligotrophic Mediterranean waters, PISCES underestimates tPOC between 0–1000 m except for the deep Chla maximum, where it overestimates tPOC. The prominent deep POC maximum simulated by PISCES is generally not found in observations from the STG biome (Fig. 7 and S9), where deep Chla maxima generally reflect phytoplankton photoacclimation, not enhanced phytoplankton biomass (Cornec et al., 2021). Thus, PISCES possibly overestimates the productivity of deep Chla maxima globally, indirectly causing stronger nutrient limitation at the surface.
690 Between the deep Chla maximum and 200 m, POC pools decrease more steeply in PISCES than in BGC-Argo observations. Between 200 and 700 m, by contrast, simulated sPOC and bPOC T_{eff} are only 10% lower than observations, well within observation uncertainty. Thus, the mesopelagic sPOC deficit simulated by PISCES in the STG originates mostly through the insufficient vertical POC export at 200 m depth. The Mediterranean represents a different case, whereby the large disagreement between PISCES and BGC-Argo T_{eff} may result from either poorly constrained POC/b_{bp700} , simulated POC
695 dynamics, or both. Thus, this region may provide a good testbed for studying the role of the mineral fraction in the BCP, including the controversial ballast hypothesis (Francois et al., 2002; Klaas and Archer, 2002; Passow, 2004).

In summary, the mismatch with observations suggests the need to improve the representation of sPOC–bPOC interconversion in PISCES. The size distribution of POC along the vertical axis is a key variable for constraining POC
700 budgets, because it reflects the interplay between gravitational sinking, remineralization, trophic transfer and 3D dynamics including horizontal POC advection (Alonso-González et al., 2009; Boyd et al., 2019). In many instances (Fig. 9), our analysis suggests that better model performance in the mesopelagic may be achieved by increasing the net transfer of bPOC to sPOC and the T_{eff} of both fractions, which may require further balancing the interplay between various mechanisms of POC export and flux attenuation. The vertical model-observations mismatch patterns observed here emphasize that POC
705 budgets have to be computed with the highest vertical resolution affordable, or otherwise an apparent POC budget balance may result from compensating imbalances in different horizons (Giering et al., 2014; Marsay et al., 2015). The detailed level of information available from BGC-Argo floats may prove to be extremely valuable to help improve the POC schemes embedded in models such as PISCES.



5. Conclusions and outlook

710 In this study we compared globally distributed POC observations between 0–1000 m made by BGC-Argo floats to the
predictions made by the PISCES model (PISCESv2). A subset of BGC-Argo floats profiling at high vertical resolution
enabled us to analyze small and big POC separately. The comparisons rely on a proposed new scheme for converting a bio-
optical measurement (b_{bp700}) to POC. Although PISCES recreates with good skill the main features observed in subpolar and
715 subtropical biomes, the comparison is still hampered by: (1) spatial and temporal variability in POC/ b_{bp700} conversion
factors, (2) mismatches in observed and simulated physics, and (3) imperfect correspondence between observed and
simulated POC fractions. Evaluation of these uncertainties allowed us to detect limitations of the biogeochemical model
parameterizations, which may arise from both suboptimal model parameters and model structure. Therefore, the descriptive
work and model-data matching strategies presented here pave the way towards the use of BGC-Argo observations for data
assimilation and model parameter optimization (Falls et al., *submitted*) and, ultimately, model development.

720

Widespread use of BGC-Argo data for understanding POC budgets and the BCP can complement classical model constraints
based on vertical POC fluxes and ocean-interior nutrient remineralization. Merging of BGC-Argo and satellite data streams
through data-driven approaches—which allow for great flexibility—, and mechanistic models—which provide process-
level understanding—, can soon provide us with a high-resolution 4D view of the oceanic carbon cycle. Further work is
725 granted to investigate POC dynamics through combination of PISCES2 and autonomous observations.

Below we list several research priorities, whose implementation would advance the study of the biological carbon pump
through the synergies between BGC-Argo observations and modelling.

- Observations:

- 730 ○ High-resolution bio-optical profiles are indispensable for process-level understanding. Combination of
low- and high-resolution sampling in separate or individual floats (e.g. burst sampling) may provide a good
compromise between float lifetime and observation capabilities.
- More in situ collocated measurements of chemical and bio-optical variables are needed to constrain b_{bp700} -
POC conversion factors, especially in meso- and bathypelagic waters.
- 735 ○ Inclusion of new sensors (e.g. Claustre et al. (2020) and extension of measurements into the bathypelagic
(Deep-Argo; e.g. Roemmich et al., 2019) hold high potential for advancing BCP research.
- Further developments in BGC-Argo data processing are needed, with the final goal of supplying a wide
public with user-friendly data products in near real time.

- Models:

- 740 ○ Evaluating model skill at resolving POC stocks, in addition to fluxes, is key to ensure that models
reproduce observed fluxes for the right reasons.



- Evaluation against globally consistent datasets is critical to avoid model overtuning towards small, sparse datasets, such as vertical POC fluxes.
- Continuous development of schemes representing particle dynamics across the entire size spectrum is needed to constrain ecologically, climatically and economically relevant element fluxes.
- Extension of prognostic modelling of bio-optical properties (Dutkiewicz et al., 2019) into the meso- and bathypelagic layers would enable direct matching with measurements made from autonomous platforms, facilitating their assimilation by models.
- Joint planning of field observation and modelling projects, from their very conception and through their entire development, is key to fully exploit the capabilities of each approach.

Data availability. The simulated and observed datasets analyzed in this article are available at <https://doi.org/10.5281/zenodo.5139602>. The code and documentation of NEMO and PISCES are available at <https://www.nemo-ocean.eu/>. The authors can provide the code used to process the datasets on reasonable request.

Supplement. A supplement with 16 figures (Fig. S1–S16) and one table (Table S1) is available.

Author contributions. M.G. and R.B. designed the study. M.F. produced and/or reprocessed global climatological datasets. R.B. produced the NEMO dynamical fields used to force PISCES 1D offline simulations. O.A. provided the global PISCES simulation. M.G processed BGC-Argo coherent annual time series, ran PISCES 1D simulations, analyzed data and produced the figures, and wrote the manuscript with contributions from all coauthors.

Competing interests. The authors declare no conflict of interest.

Acknowledgments. The authors acknowledge Antoine Poteau for guidance with BGC-Argo data; Margarida Samsó and Pierre-Antoine Bretonnière for downloading and storing the Argo data; and Thomas Arsouze, Vladimir Lapin and Joan Llorc for advice on the PISCES 1D configuration. Argo data were collected and made freely available by the International Argo Program, which is part of the Global Ocean Observing System, and the national programs that contribute to it.

Financial support. M.G. has received financial support through the Postdoctoral Junior Leader Fellowship Programme from "La Caixa" Banking Foundation (ORCAS project; LCF/BQ/PI18/11630009) and through the OPERA project funded by the Ministerio de Ciencia, Innovación y Universidades (PID2019-107952GA-I00). R.B. acknowledges support from the Ministerio de Ciencia, Innovación y Universidades as part of the DeCUSO project (CGL2017-84493-R).



Appendix A: Calculation of POC/ b_{bp700} ratios and related optical considerations

POC/ b_{bp700} ratios at the sea surface were obtained from the slope of the linear regression between POC and b_{bp700} (Table A1). Our approach essentially follows the literature compilation made by Cetinić et al. (2012). The linear regressions generally yielded small and non-significant y intercepts for sea-surface data. Therefore, we assumed the slopes were equal to the POC/ b_{bp700} ratio. When the b_{bp} measurements were made at another wavelength, we converted them to b_{bp700} assuming an exponent $\eta = 0.41$ (Cetinić et al., 2012), according to the equation:

$$b_{bp}(\lambda_1) = b_{bp}(\lambda_0) * (\lambda_1/\lambda_0)^\eta \quad (A1)$$

For measurements taken at 555 nm, which was the wavelength used in two studies (Table A1), this resulted in 10% lower b_{bp700} compared to b_{bp555} , thus higher POC/ b_{bp700} ratios.

The dataset of Cetinić et al. (2012) was the only one showing a significant negative intercept of the POC vs. b_{bp700} linear regression. Unlike the other datasets, where the POC vs. b_{bp700} relationship reflected mostly sea-surface variability in a given biome, this was the only dataset that included data collected between the sea surface and 600 m. Bol et al. (2018) reprocessed this dataset by computing the linear regression between POC and b_{bp700} in different depth bins, forcing the intercept through zero. The slope of the POC vs. b_{bp700} regressions, and therefore the POC/ b_{bp700} ratio, decreased by more than twofold between the surface and the 600 m bins. These results suggest that the POC vs. b_{bp700} relationship may be better modelled with nonlinear equations, as done for surface data in some previous studies (Balch et al., 2010; Johnson et al., 2017; Stramski et al., 1999). However, one must keep in mind that the ecosystem processes that define POC/ b_{bp700} ratios in the surface layer may be different from those occurring in the mesopelagic (see Discussion, 4.2).

The conversion between POC and particulate beam attenuation at 660 nm, c_p , in the surface ocean has been analyzed on more occasions than its b_{bp700} counterpart. The backscattering ratio, b_{bp}/b_p , relates particulate backscattering to the total particulate scattering, and is directly related to the refractive index of the particle assemblage (Babin et al., 2003; Dall'Olmo et al., 2009; Loisel et al., 2011; Organelli et al., 2018; Stramski and Kiefer, 1991; Stramski et al., 1999; Twardowski et al., 2001; Ulloa et al., 1994). Light absorption by particles is negligible in the 650-700 nm spectral region, such that total beam attenuation c_p is a good approximation of the scattering coefficient b_p . Thus, once the known absorption and scattering coefficients of seawater are removed, b_{bp}/c_p is a good approximation of the backscattering ratio, and can be used to compare the relationships between POC vs. c_p and POC vs. b_{bp700} .

The observed POC/ b_{bp700} variability in the surface layer across biomes reflected in our POC estimation algorithm is analogous to that found for the relationship between POC/ c_p by Cetinić et al. (2012), as shown in Figure A1, although fewer POC- b_{bp700} datasets are available. The POC content per unit b_{bp700} decreases with the maximum b_{bp700} of each dataset, which may be related to the structure and species composition of upper-ocean ecosystems (see Discussion, 4.3). Given that the



805 backscattering coefficient is sensitive mostly to particles smaller than 30 μm (Organelli et al., 2018), it is also plausible that the portion of POC that contributes to backscattering varies across sites, further enhancing POC/ $b_{\text{bp}700}$ variability.

The number of studies that tackled POC vs. bio-optical conversion in the mesopelagic layer is much smaller than those that focused on the epipelagic layer. Besides Cetinić et al. (2012) in the subpolar North Atlantic, we are only aware of the study
810 of Bishop et al. (1999) in the northeast Subarctic Pacific. The latter study found a POC vs. c_p slope of $16.3 \pm 0.49 \text{ mmol C m}^{-2}$ ($= \text{mmol C m}^{-3} / \text{m}^{-1}$) over the 0–1000 m depth range (the positive regression y-intercept in that study corresponds to absorption by seawater). This slope lies in the low range of the compilation shown in Fig. A1a ($196 \pm 5.9 \text{ mg C m}^{-2}$ in mass units). A close-up into the lower measurement range (Fig. 5 of Bishop et al., 1999) shows that the slope was not clearly
815 distinct for POC concentration $< 0.5 \text{ mmol m}^{-3}$, typical of the mesopelagic layer. If we assume that the backscattering ratio was likely between 1 and 2% in the mesopelagic, then we obtain a POC/ $b_{\text{bp}700}$ ratio of 815–1630. This range is compatible with the POC/ $b_{\text{bp}700}$ of $\sim 1000 \text{ mmol C m}^{-2}$ found at 600 m by Bol. et al. 2018, which we used as the asymptotic deep POC/ $b_{\text{bp}700}$ ratio in Eq. 1. Note that the linear relationship between c_p and POC is compatible with the nonlinear relationship between POC and $b_{\text{bp}700}$ along the vertical profile if the backscattering ratio also increases with depth, as found by Cetinić et al. (2012). The latter study found an increase in the backscattering ratio ($b_{\text{bp}700}/c_{\text{p}653}$) from around 1.2% at the surface to
820 around 1.5% in the upper mesopelagic. The $b_{\text{bp}700}/c_{\text{p}653}$ ratio was more variable in deeper layers and values $> 2\%$ were not rare (see also Nencioli et al., 2010; Organelli et al., 2018; Twardowski et al., 2001).

Beyond the natural variability, the interconversion between POC and bio-optical proxies is also confounded by
825 methodological, most of which were not fully addressed in the studies compiled here. Measurement of POC in the lower mesopelagic (below 500 m) requires filtration of large sample volumes in the m^3 range (Bishop et al., 1999), otherwise POC concentration rapidly approaches the detection limit with procedures and filtration volumes used for the epipelagic and the upper mesopelagic (Cetinić et al., 2012; Strubinger-Sandoval et al., 2021).



References

- 830 Alonso-Gonzalez, I. J., Aristegui, J., Lee, C., Sanchez-Vidal, A., Calafat, A., Fabres, J., Sangra, P., Masque, P., Hernandez-Guerra, A. and Benitez-Barrios, V.: Role of slowly settling particles in the ocean carbon cycle, *Geophys. Res. Lett.*, 37(13), 1–5, doi:10.1029/2010GL043827, 2010.
- Alonso-González, I. J., Arístegui, J., Vilas, J. C. and Hernández-Guerra, A.: Lateral POC transport and consumption in surface and deep waters of the Canary Current region: A box model study, *Global Biogeochem. Cycles*, 23(2), 1–12, doi:10.1029/2008GB003185, 2009.
- Argo: Argo float data and metadata from Global Data Assembly Centre (Argo GDAC). SEANOE. [Data set], , doi:10.17882/42182, 2000.
- Aristegui, J., Gasol, J. M., Duarte, C. M. and Herndl, G. J.: Microbial oceanography of the dark ocean's pelagic realm, *Limnol. Oceanogr.*, 54(5), 1501–1529, doi:10.4319/lo.2009.54.5.1501, 2009.
- 840 Arnosti, C., Fuchs, B. M., Amann, R. and Passow, U.: Contrasting extracellular enzyme activities of particle-associated bacteria from distinct provinces of the north Atlantic Ocean, *Front. Microbiol.*, 3(DEC), 1–9, doi:10.3389/fmicb.2012.00425, 2012.
- Aumont, O., Ethé, C., Tagliabue, A., Bopp, L. and Gehlen, M.: PISCES-v2: An ocean biogeochemical model for carbon and ecosystem studies, *Geosci. Model Dev.*, 8(8), 2465–2513, doi:10.5194/gmd-8-2465-2015, 2015.
- 845 Aumont, O., Van Hulst, M., Roy-Barman, M., Dutay, J. C., Éthé, C. and Gehlen, M.: Variable reactivity of particulate organic matter in a global ocean biogeochemical model, *Biogeosciences*, 14(9), doi:10.5194/bg-14-2321-2017, 2017.
- Babin, M., Morel, A., Fournier-sicre, V., Fell, F., Stramski, D., Mar, N., Villefranche, D., Cedex, V. and Morel, A.: Light Scattering Properties of Marine Particles in Coastal and Open Ocean Waters as Related to the Particle Mass Concentration Light scattering properties of marine particles in coastal and open ocean waters as related to the particle mass concentration, *Limnology*, 48(2), 843–859, 2003.
- 850 Baker, C. A., Henson, S. A., Cavan, E. L., Giering, S. L. C. and Sanders, R.: Slow-sinking particulate organic carbon in the Atlantic Ocean: Magnitude, flux, and potential controls, *Global Biogeochem. Cycles*, 31, 1051–1065, doi:10.1002/2017GB005638, 2017.
- Balch, W. M., Bowler, B. C., Drapeau, D. T., Poulton, A. J. and Holligan, P. M.: Biominerals and the vertical flux of particulate organic carbon from the surface ocean, , 37(November), 1–6, doi:10.1029/2010GL044640, 2010.
- 855 Baltar, F., Aristegui, J., Gasol, J. M., Sintes, E., Van Aken, H. M. and Herndl, G. J.: High dissolved extracellular enzymatic activity in the deep central Atlantic ocean, *Aquat. Microb. Ecol.*, 58(3), 287–302, doi:10.3354/ame01377, 2010a.
- Baltar, F., Aristegui, J., Sintes, E., Gasol, J. M., Reinthaler, T. and Herndl, G. J.: Significance of non-sinking particulate organic carbon and dark CO₂ fixation to heterotrophic carbon demand in the mesopelagic northeast Atlantic, *Geophys. Res. Lett.*, 37(9), 1–6, doi:10.1029/2010GL043105, 2010b.
- 860 Belcher, A., Iversen, M., Giering, S., Riou, V., Henson, S. A., Berline, L., Guilloux, L. and Sanders, R.: Depth-resolved



- particle-associated microbial respiration in the northeast Atlantic, *Biogeosciences*, 13, 4927–4963, doi:10.5194/bg-13-4927-2016, 2016.
- Bellacicco, M., Cornec, M., Organelli, E., Brewin, R. J. W., Neukermans, G., Volpe, G., Barbieux, M., Poteau, A.,
865 Schmechtig, C., D’Ortenzio, F., Marullo, S., Claustre, H. and Pitarch, J.: Global Variability of Optical Backscattering by Non-algal particles From a Biogeochemical-Argo Data Set, *Geophys. Res. Lett.*, 46(16), 9767–9776, doi:10.1029/2019GL084078, 2019.
- Bishop, J. K. B., Conte, M. H., Wiebe, P. H., Roman, M. R. and Langdon, C.: Particulate matter production and consumption in deep mixed layers: observations in a warm-core ring, *Deep Sea Res. Part A, Oceanogr. Res. Pap.*, 33(11-12), 1813–1841,
870 doi:10.1016/0198-0149(86)90081-6, 1986.
- Bishop, J. K. B., Calvert, S. E. and Soon, M. Y. S.: Spatial and temporal variability of POC in the northeast subarctic Pacific, *Deep. Res. Part II Top. Stud. Oceanogr.*, 46(11-12), 2699–2733, doi:10.1016/S0967-0645(99)00081-8, 1999.
- Bishop, J. K. B., Wood, T. J., Davis, R. E. and Sherman, J. T.: Robotic Observations of Enhanced Carbon Biomass and Export at 55°S during SOFeX, *Science*, 304(5669), 417–420, doi:10.1126/science.1087717, 2004.
- 875 Bisson, K., Siegel, D. A., DeVries, T., Cael, B. B. and Buesseler, K. O.: How data set characteristics influence ocean carbon export models, *Global Biogeochem. Cycles*, (32), 1312–1328, doi:10.1029/2018GB005934, 2019.
- Bode, A., Olivar, M. P. and Hernández-León, S.: Trophic indices for micronektonic fishes reveal their dependence on the microbial system in the North Atlantic, *Sci. Rep.*, 11(1), doi:10.1038/s41598-021-87767-x, 2021.
- Bol, R., Henson, S. A., Rumyantseva, A. and Briggs, N.: High-Frequency Variability of Small-Particle Carbon Export Flux
880 in the Northeast Atlantic, *Global Biogeochem. Cycles*, 32(12), 1803–1814, doi:10.1029/2018GB005963, 2018.
- Boyd, P. W., Claustre, H., Levy, M., Siegel, D. A. and Weber, T.: Multi-faceted particle pumps drive carbon sequestration in the ocean, *Nature*, 568, 327–335, doi:10.1038/s41586-019-1098-2, 2019.
- Briggs, N., Perry, M. J., Cetinić, I., Lee, C., D’Asaro, E., Gray, A. M. and Rehm, E.: High-resolution observations of aggregate flux during a sub-polar North Atlantic spring bloom, *Deep. Res. Part I Oceanogr. Res. Pap.*, 58(10), 1031–1039,
885 doi:10.1016/j.dsr.2011.07.007, 2011.
- Briggs, N., Olmo, G. D. and Claustre, H.: Major role of particle fragmentation in regulating the biological sequestration of CO₂ by the oceans, *Science*, 793, 791–793, 2020.
- Buesseler, K. O. and Boyd, P. W.: Shedding light on processes that control particle export and flux attenuation in the twilight zone of the open ocean, *Limnol. Oceanogr.*, 54(4), 1210–1232, doi:10.4319/lo.2009.54.4.1210, 2009.
- 890 Buesseler, K. O., Boyd, P. W., Black, E. E. and Siegel, D. A.: Metrics that matter for assessing the ocean biological carbon pump, *Proc. Natl. Acad. Sci. U. S. A.*, 117(18), 9679–9687, doi:10.1073/pnas.1918114117, 2020.
- Burd, A. B., Hansell, D. A., Steinberg, D. K., Anderson, T. R., Arístegui, J., Baltar, F., Beupré, S. R., Buesseler, K. O., DeHairs, F., Jackson, G. A., Kadko, D. C., Koppelman, R., Lampitt, R. S., Nagata, T., Reinthaler, T., Robinson, C., Robison, B. H., Tamburini, C. and Tanaka, T.: Assessing the apparent imbalance between geochemical and biochemical
895 indicators of meso- and bathypelagic biological activity: What the @!\$# is wrong with present calculations of carbon



- budgets?, *Deep. Res. Part II Top. Stud. Oceanogr.*, 57(16), 1557–1571, doi:10.1016/j.dsr2.2010.02.022, 2010.
- Cael, B. B. and White, A. E.: Sinking Versus Suspended Particle Size Distributions in the North Pacific Subtropical Gyre, *Geophys. Res. Lett.*, 47(15), doi:10.1029/2020GL087825, 2020.
- Cetinić, I., Perry, M. J., Briggs, N. T., Kallin, E., D’Asaro, E. A. and Lee, C. M.: Particulate organic carbon and inherent
900 optical properties during 2008 North Atlantic bloom experiment, *J. Geophys. Res. Ocean.*, 117(6),
doi:10.1029/2011JC007771, 2012.
- Claustre, H.: Is desert dust making oligotrophic waters greener?, *Geophys. Res. Lett.*, 29(10), 10–13,
doi:10.1029/2001GL014056, 2002.
- Claustre, H., Morel, A., Babin, M., Cailliau, C., Marie, D., Marty, J. C., Tailliez, D. and Vaultot, D.: Variability in particle
905 attenuation and chlorophyll fluorescence in the tropical Pacific: Scales, patterns, and biogeochemical implications, *J.*
Geophys. Res. Ocean., 104(C2), 3401–3422, doi:10.1029/98jc01334, 1999.
- Claustre, H., Johnson, K. S. and Takeshita, Y.: Observing the Global Ocean with Biogeochemical-Argo, *Ann. Rev. Mar.*
Sci., 12(1), annurev-marine-010419-010956, doi:10.1146/annurev-marine-010419-010956, 2020.
- Cornec, M., Claustre, H., Mignot, A., Guidi, L., Lacour, L., Poteau, A., D’Ortenzio, F., Gentili, B. and Schmechtig, C.: Deep
910 Chlorophyll Maxima in the Global Ocean: Occurrences, Drivers and Characteristics, *Global Biogeochem. Cycles*, 35(4), 1–
30, doi:10.1029/2020gb006759, 2021.
- Dall’Olmo, G. and Mork, K. A.: Carbon export by small particles in the Norwegian Sea, *Geophys. Res. Lett.*, 41(8), 2921–
2927, doi:10.1002/2014GL059244, 2014.
- Dall’Olmo, G., Westberry, T. K., Behrenfeld, M. J., Boss, E. and Slade, W. H.: Significant contribution of large particles to
915 optical backscattering in the open ocean, *Biogeosciences*, 6(6), 947–967, doi:10.5194/bg-6-947-2009, 2009.
- Doney, S. C., Lindsay, K., Caldeira, K., Campin, J. M., Drange, H., Dutay, J. C., Follows, M., Gao, Y., Gnanadesikan, A.,
Gruber, N., Ishida, A., Joos, F., Madec, G., Maier-Reimer, E., Marshall, J. C., Matear, R. J., Monfray, P., Mouchet, A.,
Najjar, R., Orr, J. C., Plattner, G. K., Sarmiento, J., Schlitzer, R., Slater, R., Totterdell, I. J., Weirig, M. F., Yamanaka, Y.
and Yool, A.: Evaluating global ocean carbon models: The importance of realistic physics, *Global Biogeochem. Cycles*,
920 18(3), doi:10.1029/2003GB002150, 2004.
- Duteil, O., Koeve, W., Oschlies, A., Aumont, O., Bianchi, D., Bopp, L., Galbraith, E., Matear, R., Moore, J. K., Sarmiento,
J. L. and Segschneider, J.: Preformed and regenerated phosphate in ocean general circulation models: Can right total
concentrations be wrong?, *Biogeosciences*, 9(5), 1797–1807, doi:10.5194/bg-9-1797-2012, 2012.
- Dutkiewicz, S., Hickman, A. E., Jahn, O., Henson, S., Beaulieu, C. and Monier, E.: Ocean colour signature of climate
925 change, *Nat. Commun.*, 10(1), doi:10.1038/s41467-019-08457-x, 2019.
- Evers-King, H., Martinez-Vicente, V., Brewin, R. J. W., Dall’Olmo, G., Hickman, A. E., Jackson, T., Kostadinov, T. S.,
Krasemann, H., Loisel, H., Röttgers, R., Roy, S., Stramski, D., Thomalla, S., Platt, T. and Sathyendranath, S.: Validation and
intercomparison of ocean color algorithms for estimating particulate organic carbon in the oceans, *Front. Mar. Sci.*, 4(AUG),
1–20, doi:10.3389/fmars.2017.00251, 2017.



- 930 Falls, M., Bernardello, R., Castrillo, M., Acosta, M., Llord, J. and Galí, M.: Use of Genetic Algorithms for Ocean Model Parameter Optimisation, *Geosci. Model Dev.*, n.d.
- Fay, A. R. and McKinley, G. A.: Global open-ocean biomes: Mean and temporal variability, *Earth Syst. Sci. Data*, 6(2), 273–284, doi:10.5194/essd-6-273-2014, 2014.
- Flament, P.: A state variable for characterizing water masses and their diffusive stability: Spiciness, *Prog. Oceanogr.*, 54(1-4), 493–501, doi:10.1016/S0079-6611(02)00065-4, 2002.
- 935 Francois, R., Honjo, S., Krishfield, R. and Manganini, S.: Factors controlling the flux of organic carbon to the bathypelagic zone of the ocean, *Global Biogeochem. Cycles*, 16(4), 34–1–34–20, doi:10.1029/2001gb001722, 2002.
- Gardner, W. D., Mishonov, A. V. and Richardson, M. J.: Global POC concentrations from in-situ and satellite data, *Deep. Res. Part II Top. Stud. Oceanogr.*, 53(5-7), 718–740, doi:10.1016/j.dsr2.2006.01.029, 2006.
- 940 Gasol, J. M., del Giorgio, P. A. and Duarte, C. M.: Biomass distribution in marine planktonic communities, *Limnol. Oceanogr.*, 42(6), 1353–1363, 1997.
- Giering, S. L. C., Sanders, R., Lampitt, R. S., Anderson, T. R., Tamburini, C., Boutrif, M., Zubkov, M. V., Marsay, C. M., Henson, S. A., Saw, K., Cook, K. and Mayor, D. J.: Reconciliation of the carbon budget in the ocean’s twilight zone, *Nature*, 507(7493), 480–483, doi:10.1038/nature13123, 2014.
- 945 Goldthwait, S., Yen, J., Brown, J. and Alldredge, A.: Quantification of marine snow fragmentation by swimming euphausiids, *Limnol. Oceanogr.*, 49(4 I), 940–952, doi:10.4319/lo.2004.49.4.0940, 2004.
- Graff, J. R., Westberry, T. K., Milligan, A. J., Brown, M. B., Dall’Olmo, G., Dongen-Vogels, V. van, Reifel, K. M. and Behrenfeld, M. J.: Analytical phytoplankton carbon measurements spanning diverse ecosystems, *Deep Sea Res. Part I Oceanogr. Res. Pap.*, 102, 16–25, doi:10.1016/j.dsr.2015.04.006, 2015.
- 950 Guidi, L., Legendre, L., Reygondeau, G., Uitz, J., Stemann, L. and Henson, S. A.: A new look at ocean carbon remineralization for estimating deepwater sequestration, *Global Biogeochem. Cycles*, doi:10.1002/2014GB005063, 2015.
- Haëntjens, N., Della Penna, A., Briggs, N., Karp-Boss, L., Gaube, P., Claustre, H. and Boss, E.: Detecting Mesopelagic Organisms Using Biogeochemical-Argo Floats, *Geophys. Res. Lett.*, 47(6), doi:10.1029/2019GL086088, 2020.
- Hayes, C. T., Anderson, R. F., Fleisher, M. Q., Huang, K. F., Robinson, L. F., Lu, Y., Cheng, H., Edwards, R. L. and Moran, S. B.: 230Th and 231Pa on GEOTRACES GA03, the U.S. GEOTRACES North Atlantic transect, and implications for modern and paleoceanographic chemical fluxes, *Deep. Res. Part II Top. Stud. Oceanogr.*, 116, 29–41, doi:10.1016/j.dsr2.2014.07.007, 2015.
- 955 Henson, S. A., Sanders, R., Madsen, E., Morris, P. J., Moigne, F. Le and Quartly, G. D.: A reduced estimate of the strength of the ocean’s biological carbon pump, *Geophys. Res. Lett.*, 38, GL046735, doi:10.1029/2011GL046735, 2011.
- 960 Henson, S. A., Yool, A. and Sanders, R.: Variability in efficiency of particulate organic carbon export: A model study, *Global Biogeochem. Cycles*, 33–45, doi:10.1002/2014GB004965.Received, 2015.
- Hernández-León, S., Koppelman, R., Fraile-Nuez, E., Bode, A., Mompeán, C., Irigoien, X., Olivar, M. P., Echevarría, F., Fernández de Puelles, M. L., González-Gordillo, J. I., Cózar, A., Acuña, J. L., Agustí, S. and Duarte, C. M.: Large deep-sea



- zooplankton biomass mirrors primary production in the global ocean, *Nat. Commun.*, 11(1), doi:10.1038/s41467-020-19875-7, 2020.
- Honjo, S., Manganini, S. J., Krishfield, R. A. and Francois, R.: Particulate organic carbon fluxes to the ocean interior and factors controlling the biological pump: A synthesis of global sediment trap programs since 1983, *Prog. Oceanogr.*, 76(3), 217–285, doi:10.1016/j.pocean.2007.11.003, 2008.
- Ikenoue, T., Kimoto, K., Okazaki, Y., Sato, M., Honda, M. C., Takahashi, K., Harada, N. and Fujiki, T.: Phaeodaria: An Important Carrier of Particulate Organic Carbon in the Mesopelagic Twilight Zone of the North Pacific Ocean, *Global Biogeochem. Cycles*, 33(8), 1146–1160, doi:10.1029/2019GB006258, 2019.
- Iversen, M. H. and Ploug, H.: Ballast minerals and the sinking carbon flux in the ocean: Carbon-specific respiration rates and sinking velocity of marine snow aggregates, *Biogeosciences*, 7(9), 2613–2624, doi:10.5194/bg-7-2613-2010, 2010.
- Jiao, N., Herndl, G. J., Hansell, D. a, Benner, R., Kattner, G., Wilhelm, S. W., Kirchman, D. L., Weinbauer, M. G., Luo, T., Chen, F. and Azam, F.: Microbial production of recalcitrant dissolved organic matter: long-term carbon storage in the global ocean., *Nat. Rev. Microbiol.*, 8(8), 593–599, doi:10.1038/nrmicro2386, 2010.
- Johnson, K. S., Plant, J. N., Coletti, L. J., Jannasch, H. W., Sakamoto, C. M., Riser, S. C., Swift, D. D., Williams, N. L., Boss, E., Haëntjens, N., Talley, L. D. and Sarmiento, J. L.: Biogeochemical sensor performance in the SOCCOM profiling float array, *J. Geophys. Res. Ocean.*, doi:10.1002/2017JC012838, 2017.
- Karthäuser, C., Ahmerkamp, S., Marchant, H. K., Bristow, L. A., Hauss, H., Iversen, M. H., Kiko, R., Maerz, J., Lavik, G. and Kuypers, M. M. M.: Small sinking particles control anammox rates in the Peruvian oxygen minimum zone, *Nat. Commun.*, 12(1), doi:10.1038/s41467-021-23340-4, 2021.
- Kelley, D.: Package “oce”: Analysis of Oceanographic data, R Packag. [online] Available from: <http://dankelley.github.com/oce/>, 2011.
- Kharbush, J. J., Close, H. G., Van Mooy, B. A. S., Arnosti, C., Smittenberg, R. H., Le Moigne, F. A. C., Mollenhauer, G., Scholz-Böttcher, B., Obrecht, I., Koch, B. P., Becker, K. W., Iversen, M. H. and Mohr, W.: Particulate Organic Carbon Deconstructed: Molecular and Chemical Composition of Particulate Organic Carbon in the Ocean, *Front. Mar. Sci.*, 7, doi:10.3389/fmars.2020.00518, 2020.
- Kjørboe, T.: How zooplankton feed: Mechanisms, traits and trade-offs, *Biol. Rev.*, 86(2), 311–339, doi:10.1111/j.1469-185X.2010.00148.x, 2011.
- Klaas, C. and Archer, D. E.: Association of sinking organic matter with various types of mineral ballast in the deep sea: Implications for the rain ratio, *Global Biogeochem. Cycles*, 16(4), 63–1–63–14, doi:10.1029/2001gb001765, 2002.
- Kriest, I., Kähler, P., Koeve, W., Kvale, K., Sauerland, V. and Oschlies, A.: One size fits all? Calibrating an ocean biogeochemistry model for different circulations, *Biogeosciences*, 17(12), 3057–3082, doi:10.5194/bg-17-3057-2020, 2020.
- Kwon, E. Y., Primeau, F. and Sarmiento, J. L.: The impact of remineralization depth on the air-sea carbon balance, *Nat. Geosci.*, 2(9), 630–635, doi:10.1038/ngeo612, 2009.
- Lacour, L., Briggs, N., Claustre, H., Ardyna, M. and Dall’Olmo, G.: The Intraseasonal Dynamics of the Mixed Layer Pump



- in the Subpolar North Atlantic Ocean: A Biogeochemical-Argo Float Approach, *Global Biogeochem. Cycles*, 33(3), 266–281, doi:10.1029/2018GB005997, 2019.
- 1000 Lam, P. J., Doney, S. C. and Bishop, J. K. B.: The dynamic ocean biological pump: Insights from a global compilation of particulate organic carbon, CaCO₃, and opal concentration profiles from the mesopelagic, *Global Biogeochem. Cycles*, 25(3), 1–14, doi:10.1029/2010GB003868, 2011.
- Lam, P. J., Ohnemus, D. C. and Auro, M. E.: Size-fractionated major particle composition and concentrations from the US GEOTRACES North Atlantic Zonal Transect, *Deep. Res. Part II Top. Stud. Oceanogr.*, 116, 303–320,
1005 doi:10.1016/j.dsr2.2014.11.020, 2015.
- Lampitt, R. S., Wishner, K. F., Turley, C. M. and Angel, M. V.: Marine snow studies in the Northeast Atlantic Ocean: distribution, composition and role as a food source for migrating plankton, *Mar. Biol. Int. J. Life Ocean. Coast. Waters*, 116(4), 689–702, doi:10.1007/BF00355486, 1993.
- Laufkötter, C., Vogt, M., Gruber, N., Aumont, O., Bopp, L., Doney, S. C., Dunne, J. P., Hauck, J., John, J. G., Lima, I. D.,
1010 Seferian, R. and Völker, C.: Projected decreases in future marine export production: The role of the carbon flux through the upper ocean ecosystem, *Biogeosciences*, 13(13), 4023–4047, doi:10.5194/bg-13-4023-2016, 2016.
- Laws, E. A., Falkowski, P. G., Smith, W. O., Ducklow, H. and McCarthy, J. J.: Temperature effects on export production in the open ocean, *Global Biogeochem. Cycles*, 14(4), 1231–1246, doi:10.1029/1999GB001229, 2000.
- Lee, S., Kang, Y. C. and Fuhrman, J. A.: Imperfect retention of natural bacterioplankton cells by glass fiber filters, *Mar.*
1015 *Ecol. Prog. Ser.*, 119(1-3), 285–290, doi:10.3354/meps119285, 1995.
- Legendre, L., Rivkin, R. B., Weinbauer, M. G., Guidi, L. and Uitz, J.: The microbial carbon pump concept: Potential biogeochemical significance in the globally changing ocean, *Prog. Oceanogr.*, 134, 432–450, doi:10.1016/j.pocean.2015.01.008, 2015.
- Llort, J., Lévy, M., Sallée, J.-B. and Tagliabue, A.: Onset, intensification, and decline of phytoplankton blooms in the
1020 Southern Ocean, *ICES J. Mar. Sci.*, 72(6), 1971–1984, doi:10.1093/icesjms/fst176, 2015.
- Llort, J., Langlais, C., Matear, R., Moreau, S., Lenton, A. and Strutton, P. G.: Evaluating Southern Ocean Carbon Eddy-Pump From Biogeochemical Argo Floats, *J. Geophys. Res. Ocean.*, 1–14, doi:10.1002/2017JC012861, 2018.
- Loisel, H. and Morel, A.: Light Scattering and Chlorophyll Concentration in Case 1 Waters: A Reexamination, *Limnol. Oceanogr.*, 43(5), 847–858, doi:10.4319/lo.1998.43.5.0847, 1998.
- 1025 Loisel, H., Vantrepotte, V., Norkvist, K., Mrioux, X., Kheireddine, M., Ras, J., Pujo-Pay, M., Combet, Y., Leblanc, K., Dall’Olmo, G., Mauriac, R., Dessailly, D. and Moutin, T.: Characterization of the bio-optical anomaly and diurnal variability of particulate matter, as seen from scattering and backscattering coefficients, in ultra-oligotrophic eddies of the Mediterranean Sea, *Biogeosciences*, 8(11), 3295–3317, doi:10.5194/bg-8-3295-2011, 2011.
- Löptien, U. and Dietze, H.: Reciprocal bias compensation and ensuing uncertainties in model-based climate projections:
1030 Pelagic biogeochemistry versus ocean mixing, *Biogeosciences*, 16(9), 1865–1881, doi:10.5194/bg-16-1865-2019, 2019.
- Marsay, C. M., Sanders, R. J., Henson, S. A., Pabortsava, K., Achterberg, E. P. and Lampitt, R. S.: Attenuation of sinking



- particulate organic carbon flux through the mesopelagic ocean, *Proc. Natl. Acad. Sci.*, 112(4), 1089–1094, doi:10.1073/pnas.1415311112, 2015.
- Martin, J. H., Knauer, G. A., Karl, D. M. and Broenkow, W. W.: VERTEX: carbon cycling in the northeast Pacific, *Deep Res.*, 34(2), 267–285, 1987.
- Mayor, D. J., Gentleman, W. C. and Anderson, T. R.: Ocean carbon sequestration: Particle fragmentation by copepods as a significant unrecognised factor?, *BioEssays*, 42(12), 2000149, doi:10.1002/bies.202000149, 2020.
- Menden-Deuer, S. and Lessard, E. J.: Carbon to volume relationships for dinoflagellates, diatoms, and other protist plankton, *Limnol. Oceanogr.*, 45(3), 569–579, doi:10.4319/lo.2000.45.3.0569, 2000.
- 1040 Moore, T. S., Dowell, M. D. and Franz, B. A.: Detection of coccolithophore blooms in ocean color satellite imagery: A generalized approach for use with multiple sensors, *Remote Sens. Environ.*, 117, 249–263, doi:10.1016/j.rse.2011.10.001, 2012.
- Morán, X. A. G., Gasol, J. M., Arin, L. and Estrada, M.: A comparison between glass fiber and membrane filters for the estimation of phytoplankton POC and DOC production, *Mar. Ecol. Prog. Ser.*, 187, 31–41, 1999.
- 1045 Nencioli, F., Chang, G., Twardowski, M. and Dickey, T. D.: Optical characterization of an eddy-induced diatom bloom west of the island of Hawaii, *Biogeosciences*, 7(1), 151–162, doi:10.5194/bg-7-151-2010, 2010.
- Omand, M. M., D’Asaro, E. A., Lee, C. M., Perry, M. J., Briggs, N., Cetini, I. and Mahadevan, A.: Eddy-driven subduction exports particulate organic carbon from the spring bloom, *Science*, 348(6231), 222–225, doi:10.1126/science.1260062, 2015.
- Organelli, E., Dall’Olmo, G., Brewin, R. J. W., Tarran, G. A., Boss, E. and Bricaud, A.: The open-ocean missing
1050 backscattering is in the structural complexity of particles, *Nat. Commun.*, 9(1), doi:10.1038/s41467-018-07814-6, 2018.
- Organelli, E., Dall’Olmo, G., Brewin, R. J. W., Nencioli, F. and Tarran, G. A.: Drivers of spectral optical scattering by particles in the upper 500 m of the Atlantic Ocean, *Opt. Express*, 28(23), 34147, doi:10.1364/oe.408439, 2020.
- Oschlies, A., Brandt, P., Stramma, L. and Schmidtko, S.: Drivers and mechanisms of ocean deoxygenation, *Nat. Geosci.*, 11, 467–473, doi:10.1038/s41561-018-0152-2, 2018.
- 1055 Oubelkheir, K., Claustre, H., Sciandra, A. and Babin, M.: Bio-optical and biogeochemical properties of different trophic regimes in oceanic waters, *Limnol. Oceanogr.*, 50(6), 1795–1809, doi:10.4319/lo.2005.50.6.1795, 2005.
- Pachiadaki, M. G., Sintes, E., Bergauer, K., Brown, J. M., Record, N. R., Swan, B. K., Mathyer, M. E., Hallam, S. J., Lopez-Garcia, P., Takaki, Y., Nunoura, T., Woyke, T., Herndl, G. J. and Stepanauskas, R.: Major role of nitrite-oxidizing bacteria in dark ocean carbon fixation, *Science*, 358(6366), 1046–1051, doi:10.1126/science.aan8260, 2017.
- 1060 Palevsky, H. I. and Doney, S. C.: How Choice of Depth Horizon Influences the Estimated Spatial Patterns and Global Magnitude of Ocean Carbon Export Flux, *Geophys. Res. Lett.*, 45(9), 4171–4179, doi:10.1029/2017GL076498, 2018.
- Passow, U.: Switching perspectives: Do mineral fluxes determine particulate organic carbon fluxes or vice versa?, *Geochemistry, Geophys. Geosystems*, 5(4), doi:10.1029/2003GC000670, 2004.
- Poteau, A., Boss, E. and Claustre, H.: Particulate concentration and seasonal dynamics in the mesopelagic ocean based on
1065 the backscattering coefficient measured with Biogeochemical-Argo floats, *Geophys. Res. Lett.*, 44(13), 6933–6939,



- doi:10.1002/2017GL073949, 2017.
- Resplandy, L., Lévy, M. and McGillicuddy, D. J.: Effects of Eddy-Driven Subduction on Ocean Biological Carbon Pump, *Global Biogeochem. Cycles*, 33(8), 1071–1084, doi:10.1029/2018GB006125, 2019.
- Roemmich, D., Alford, M. H., Claustre, H., Johnson, K. S., King, B., Moum, J., Oke, P. R., Owens, W. B., Pouliquen, S.,
1070 Purkey, S., Scanderbeg, M., Suga, T., Wijffels, S. E., Zilberman, N., Bakker, D., Baringer, M. O., Belbeoch, M., Bittig, H.
C., Boss, E., Calil, P., Carse, F., Carval, T., Chai, F., Conchubhair, D. O., D’Ortenzio, F., Dall’Olmo, G., Desbruyères, D.,
Fennel, K., Fer, I., Ferrari, R., Forget, G., Freeland, H., Fujiki, T., Gehlen, M., Greenan, B., Hallberg, R., Hibiya, T.,
Hosoda, S., Jayne, S., Jochum, M., Johnson, G. C., Kang, K. R., Kolodziejczyk, N., Koertzing, A., Le Traon, P. Y., Lenn,
Y. D., Maze, G., Mork, K. A., Morris, T., Nagai, T., Nash, J., Garabato, A. N., Olsen, A., Pattabhi, R. R., Prakash, S., Riser,
1075 S., Schmechtig, C., Shroyer, E., Sterl, A., Sutton, P., Talley, L., Tanhua, T., Thierry, V., Thomalla, S., Toole, J., Troisi, A.,
Trull, T., Turton, J. D., Velez-Belchi, P. J., Walczowski, W., Wang, H., Wanninkhof, R., Waterhouse, A., Watson, A.,
Wilson, C., Wong, A. P., Xu, J. and Yasuda, I.: On the future of Argo: A global, full-depth, multi-disciplinary array, *Front.
Mar. Sci.*, 6(JUL), doi:10.3389/fmars.2019.00439, 2019.
- Sarmiento, J. and Gruber, N.: *Organic Matter Export and Remineralization*, in *Ocean Biogeochemical Dynamics*, pp. 173–
1080 226, Princeton University Press, Princeton, New Jersey., 2006.
- Sauzède, R., Johnson, J. E., Claustre, H., Camps-Valls, G. and Ruescas, A. B.: Estimation of Oceanic Particulate Organic
Carbon with Machine Learning, *ISPRS Ann. Photogramm. Remote Sens. Spat. Inf. Sci.*, 5(2), 949–956, doi:10.5194/isprs-
annals-V-2-2020-949-2020, 2020.
- Sauzède, R., Johnson, J., Claustre, H., Camps-Valls, G. and Ruescas, A.: MULTIOBS_GLO_BIO_BGC_3D_REP_015_010
1085 [Data set], 2021.
- Schmechtig, C., Thierry, V. and The Bio Argo Team: *Argo quality control manual for biogeochemical data.*, 2016.
- Schmechtig, C., Poteau, A., Claustre, H., D’Ortenzio, F., Dall’Olmo, G. and Boss, E. S.: Processing BGC-Argo particle
backscattering at the DAC level. [online] Available from: <http://dx.doi.org/10.13155/39459>, 2018.
- van Sebille, E., Griffies, S. M., Abernathey, R., Adams, T. P., Berloff, P., Biastoch, A., Blanke, B., Chassignet, E. P., Cheng,
1090 Y., Cotter, C. J., Deleersnijder, E., Döös, K., Drake, H. F., Drijfhout, S., Gary, S. F., Heemink, A. W., Kjellsson, J.,
Koszalka, I. M., Lange, M., Lique, C., MacGilchrist, G. A., Marsh, R., Mayorga Adame, C. G., McAdam, R., Nencioli, F.,
Paris, C. B., Piggott, M. D., Polton, J. A., Rühs, S., Shah, S. H. A. M., Thomas, M. D., Wang, J., Wolfram, P. J., Zanna, L.
and Zika, J. D.: Lagrangian ocean analysis: Fundamentals and practices, *Ocean Model.*, 121, 49–75,
doi:10.1016/j.ocemod.2017.11.008, 2018.
- 1095 Séférian, R., Berthet, S., Yool, A., Palmiéri, J., Bopp, L., Tagliabue, A., Kwiatkowski, L., Aumont, O., Christian, J., Dunne,
J., Gehlen, M., Ilyina, T., John, J. G., Li, H., Long, M. C., Luo, J. Y., Nakano, H., Romanou, A., Schwinger, J., Stock, C.,
Santana-Falcón, Y., Takano, Y., Tjiputra, J., Tsujino, H., Watanabe, M., Wu, T., Wu, F. and Yamamoto, A.: Tracking
Improvement in Simulated Marine Biogeochemistry Between CMIP5 and CMIP6, *Curr. Clim. Chang. Reports*, 6(3), 95–
119, doi:10.1007/s40641-020-00160-0, 2020.



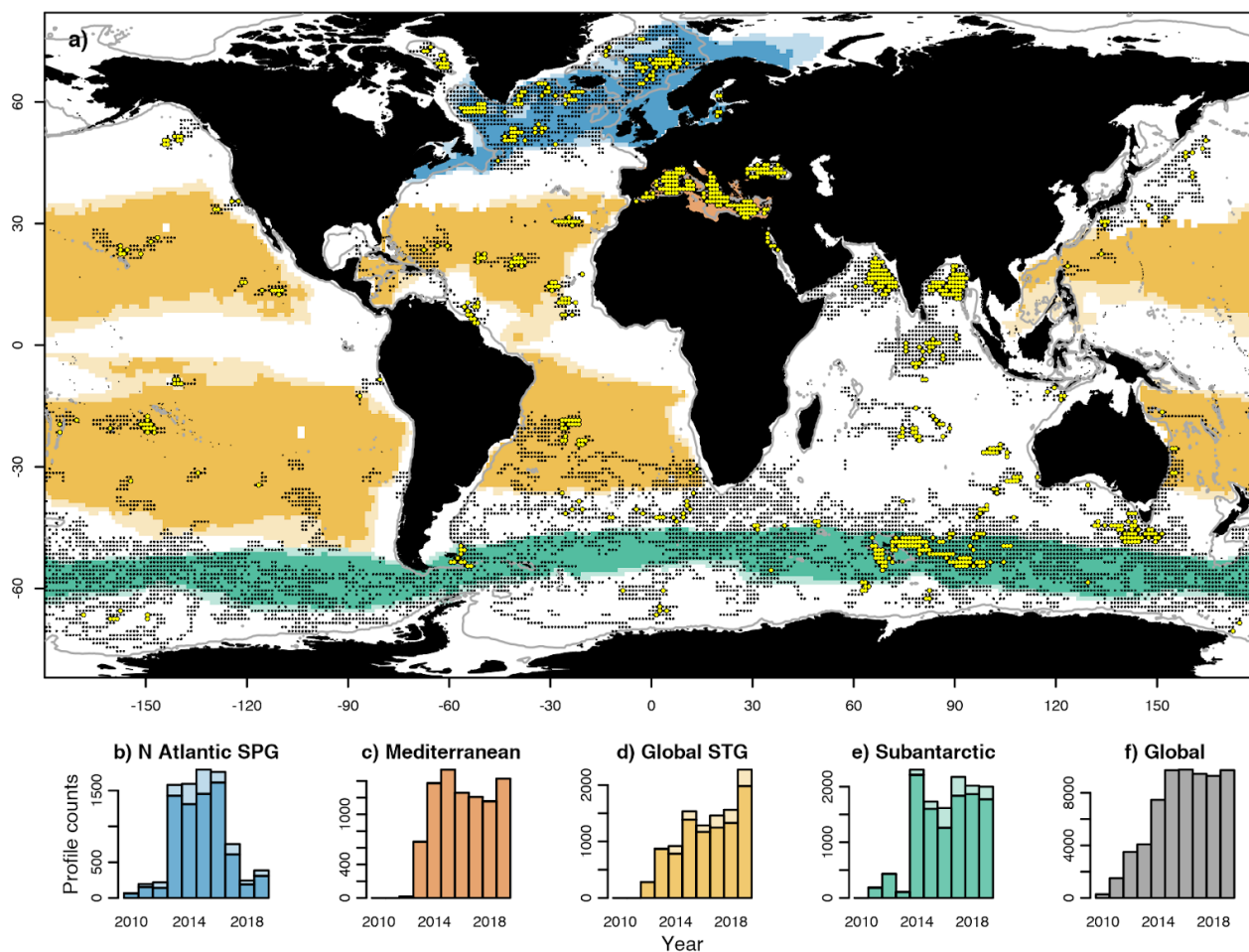
- 1100 Siegel, D. A. and Deuser, W. G.: Trajectories of sinking particles in the Sargasso Sea: Modeling of statistical funnels above deep-ocean sediment traps, *Deep. Res. Part I Oceanogr. Res. Pap.*, 44(9-10), 1519–1541, doi:10.1016/S0967-0637(97)00028-9, 1997.
- Siegel, D. A., Buesseler, K. O., Doney, S. C., Sailley, S. F., Behrenfeld, M. J. and Boyd, P. W.: Global assessment of ocean carbon export by combining satellite observations and food-web model, *Global Biogeochem. Cycles*, 28, 181–196, 1105 doi:10.1002/2013GB004743. Received, 2014.
- Steinberg, D. K., Van Mooy, B. A. S., Buesseler, K. O., Boyd, P. W., Kobari, T. and Karl, D. M.: Bacterial vs. zooplankton control of sinking particle flux in the ocean's twilight zone, *Limnol. Oceanogr.*, 53(4), 1327–1338, doi:10.4319/lo.2008.53.4.1327, 2008.
- Stemmann, L. and Boss, E.: Plankton and Particle Size and Packaging: From Determining Optical Properties to Driving the 1110 Biological Pump, *Ann. Rev. Mar. Sci.*, 4, 263–290, doi:10.1146/annurev-marine-120710-100853, 2012.
- Stemmann, L., Jackson, G. A. and Ianson, D.: A vertical model of particle size distributions and fluxes in the midwater column that includes biological and physical processes - Part I: Model formulation, *Deep. Res. Part I Oceanogr. Res. Pap.*, 51(7), 865–884, doi:10.1016/j.dsr.2004.03.001, 2004a.
- Stemmann, L., Jackson, G. A. and Gorsky, G.: A vertical model of particle size distributions and fluxes in the midwater 1115 column that includes biological and physical processes - Part II: Application to a three year survey in the NW Mediterranean Sea, *Deep. Res. Part I Oceanogr. Res. Pap.*, 51(7), 885–908, doi:10.1016/j.dsr.2004.03.002, 2004b.
- Stemmann, L., Prieur, L., Legendre, L., Taupier-Letage, I., Picheral, M., Guidi, L. and Gorsky, G.: Effects of frontal processes on marine aggregate dynamics and fluxes: An interannual study in a permanent geostrophic front (NW Mediterranean), *J. Mar. Syst.*, 70(1-2), 1–20, doi:10.1016/j.jmarsys.2007.02.014, 2008.
- 1120 Stramski, D. and Kiefer, D.: Light scattering by microorganisms in the open ocean, *Prog. Oceanogr.*, 28(4), 343–383, doi:10.1016/0079-6611(91)90032-H, 1991.
- Stramski, D., Reynolds, R. A., Kahru, M. and Mitchell, B. G.: Estimation of particulate organic carbon in the ocean from satellite remote sensing, *Science*, 285(5425), 239–242, doi:10.1126/science.285.5425.239, 1999.
- Stramski, D., Reynolds, R. a., Babin, M., Kaczmarek, S., Lewis, M. R., Röttgers, R., Sciandra, A., Stramska, M., 1125 Twardowski, M. S. and Claustre, H.: Relationships between the surface concentration of particulate organic carbon and optical properties in the eastern South Pacific and eastern Atlantic Oceans, *Biogeosciences*, 5, 171–201, doi:10.5194/bg-5-171-2008, 2008.
- Strubinger Sandoval, P., Dall'Olmo, G., Rasse, R., Ross, J. and Haines, K.: Uncertainties of particulate organic carbon concentrations in the mesopelagic zone of the Atlantic ocean, *Open Res. Eur.*, 1, 43, 2021.
- 1130 Stukel, M. R., Ohman, M. D., Kelly, T. B. and Biard, T.: The roles of suspension-feeding and flux-feeding zooplankton as gatekeepers of particle flux into the mesopelagic ocean in the Northeast Pacific, *Front. Mar. Sci.*, 6(JUL), 1–16, doi:10.3389/fmars.2019.00397, 2019.
- Terzić, E., Lazzari, P., Organelli, E., Solidoro, C., Salon, S., Ortenzio, F. D. and Conan, P.: Merging bio-optical data from



- Biogeochemical-Argo floats and models in marine biogeochemistry, *Biogeosciences*, 16, 2527–2542, 2019.
- 1135 Trudnowska, E., Lacour, L., Ardyna, M., Rogge, A., Irisson, J. O., Waite, A. M., Babin, M. and Stemmann, L.: Marine snow morphology illuminates the evolution of phytoplankton blooms and determines their subsequent vertical export, *Nat. Commun.*, 12(1), doi:10.1038/s41467-021-22994-4, 2021.
- Twardowski, M. S., Boss, E., Macdonald, J. B., Pegau, W. S., Barnard, A. H. and Zaneveld, J. R. V: A model for estimating bulk refractive index from the optical backscattering ratio and the implications for understanding particle composition in case I and case II waters, *J. Geophys. Res.*, 106(C7), 14129–14142, doi:10.1029/2000JC000404, 2001.
- 1140 Uitz, J., Claustre, H., Morel, A. and Hooker, S. B.: Vertical distribution of phytoplankton communities in open ocean: An assessment based on surface chlorophyll, *J. Geophys. Res.*, 111(C8), doi:10.1029/2005JC003207, 2006.
- Ulloa, O., Sathyendranath, S. and Platt, T.: Effect of the particle-size distribution on the backscattering ratio in seawater, *Appl. Opt.*, 33(30), 7070, doi:10.1364/ao.33.007070, 1994.
- 1145 Weber, T., Cram, J. A., Leung, S. W., DeVries, T. and Deutsch, C.: Deep ocean nutrients imply large latitudinal variation in particle transfer efficiency, *Proc. Natl. Acad. Sci.*, 113(31), doi:10.1073/pnas.1604414113, 2016.
- Wong, A., Keeley, R., Carval, T. and Argo Data Management Team: Argo Quality Control Manual for CTD and Trajectory Data., 2021.
- Woodstock, M. S., Sutton, T. T., Frank, T. and Zhang, Y.: An early warning sign: trophic structure changes in the oceanic Gulf of Mexico from 2011—2018, *Ecol. Modell.*, 445, doi:10.1016/j.ecolmodel.2021.109509, 2021.
- 1150



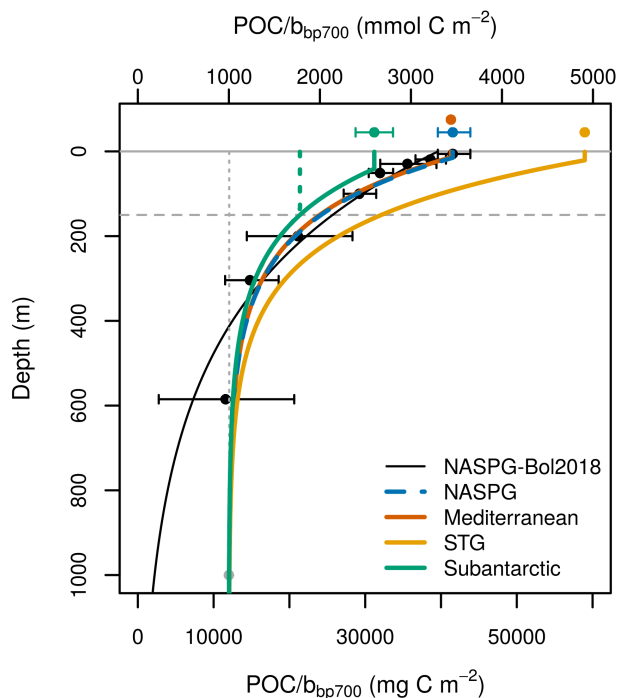
Figures



1155

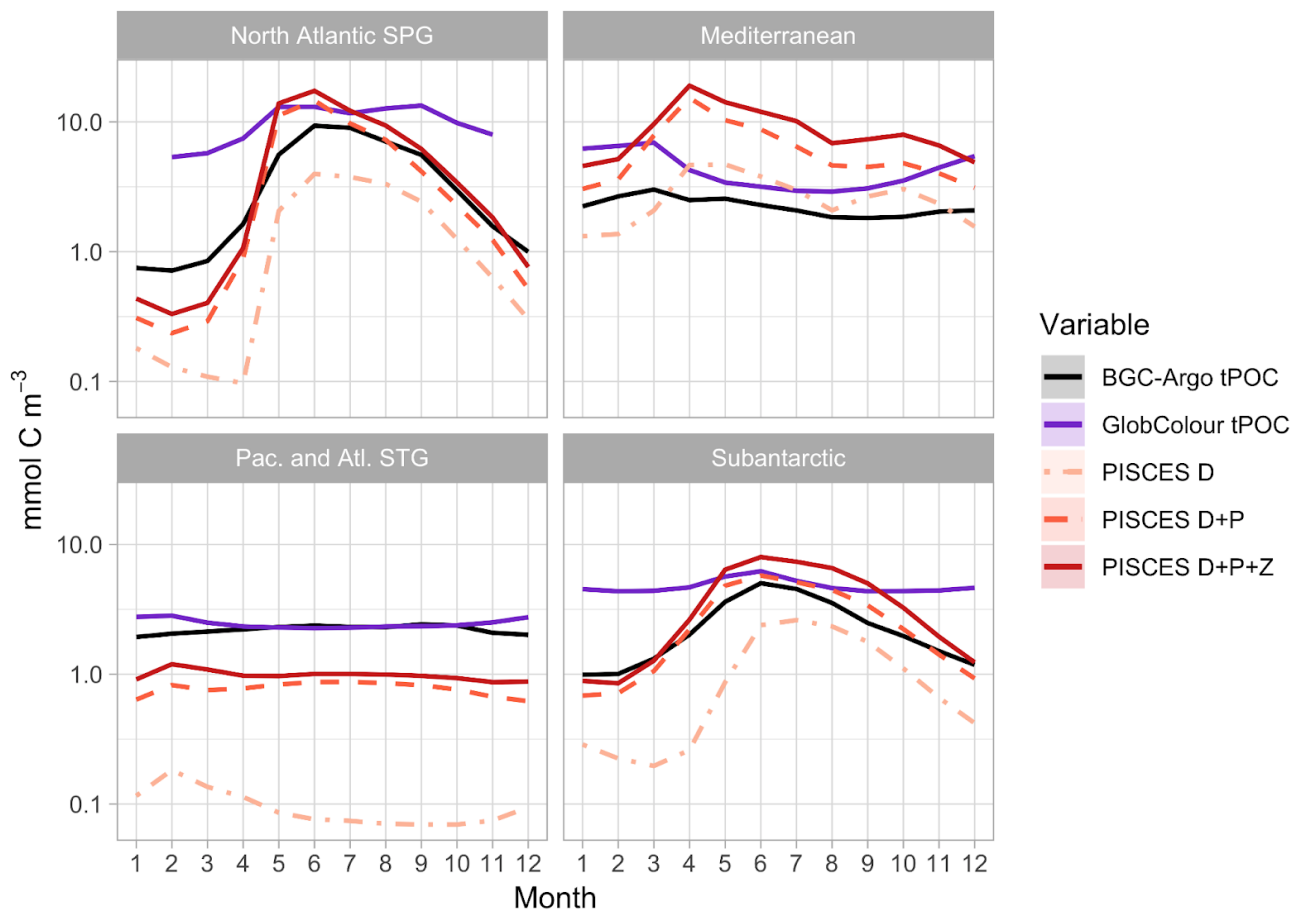
Figure 1. Global distribution and abundance of BGC-Argo profiles between 2010 and 2019. Grid cells ($1^\circ \times 1^\circ$) with at least 1 profile of the backscattering coefficient at 700 nm (b_{bp700}) are marked with black dots, and those with at least 20 profiles are marked with yellow-filled circles. The gray contours indicate the 1000 m isobath. Color shading indicates ocean biomes (see text), whose names are indicated on top of the bottom histograms. For each biome, light color indicates its average extent over 13 years of satellite observations (1998-2010), whereas the darker color indicates the “core” grid cells that never changed biome classification during the same period. Bottom panels (b-f) show the number of BGC-Argo b_{bp700} profiles per year in the four selected biomes and in the global ocean.

1160

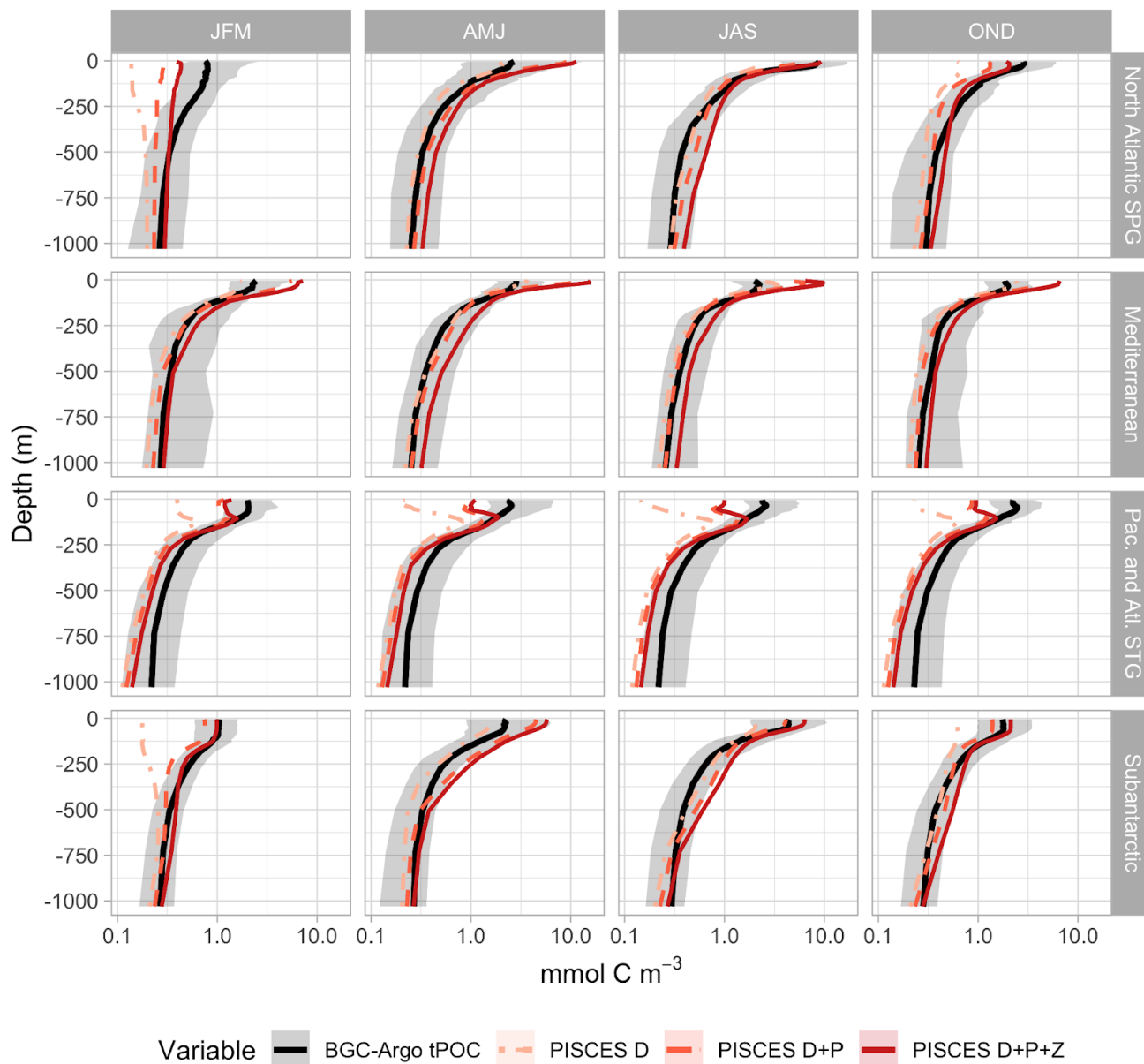


1165 **Figure 2. Empirical model used to convert the backscattering coefficient at 700 nm (bbp_{700}) to particulate organic carbon (POC). Black dots and error bars show the dataset of Cetinić et al. (2012) as binned by Bol et al. (2018). The black curve shows the exponential fit of Bol et al. (2018) to the Cetinić dataset. The blue curve shows our fit to the same dataset (NASPG: North Atlantic Subpolar Gyre), forced to converge to a nonzero minimum value at depth. The remaining curves show similar functions with the same exponential slope ($b = -6.57$) as the NASPG fit, but with different surface values derived from the following studies: Loisel et al. (2001) for the Mediterranean Sea; Stramski et al. (2008) for the ensemble of subtropical and tropical areas excluding equatorial upwellings (STG); and Johnson et al. (2017) for the Southern Ocean (Subantarctic). The depth of the homogeneous surface layer, $z_{surf,biome}$ in Eq. 1 and 2, corresponds to the 5% quantile of the climatological MLD in summer in a given biome: 15 m in the NASPG, 14 m in the MED, 21 m in the STG and 41 m in the SO. The dotted green line, shown for the SO case only, illustrates the behavior of the algorithm for a mixed layer depth of 150 m.**

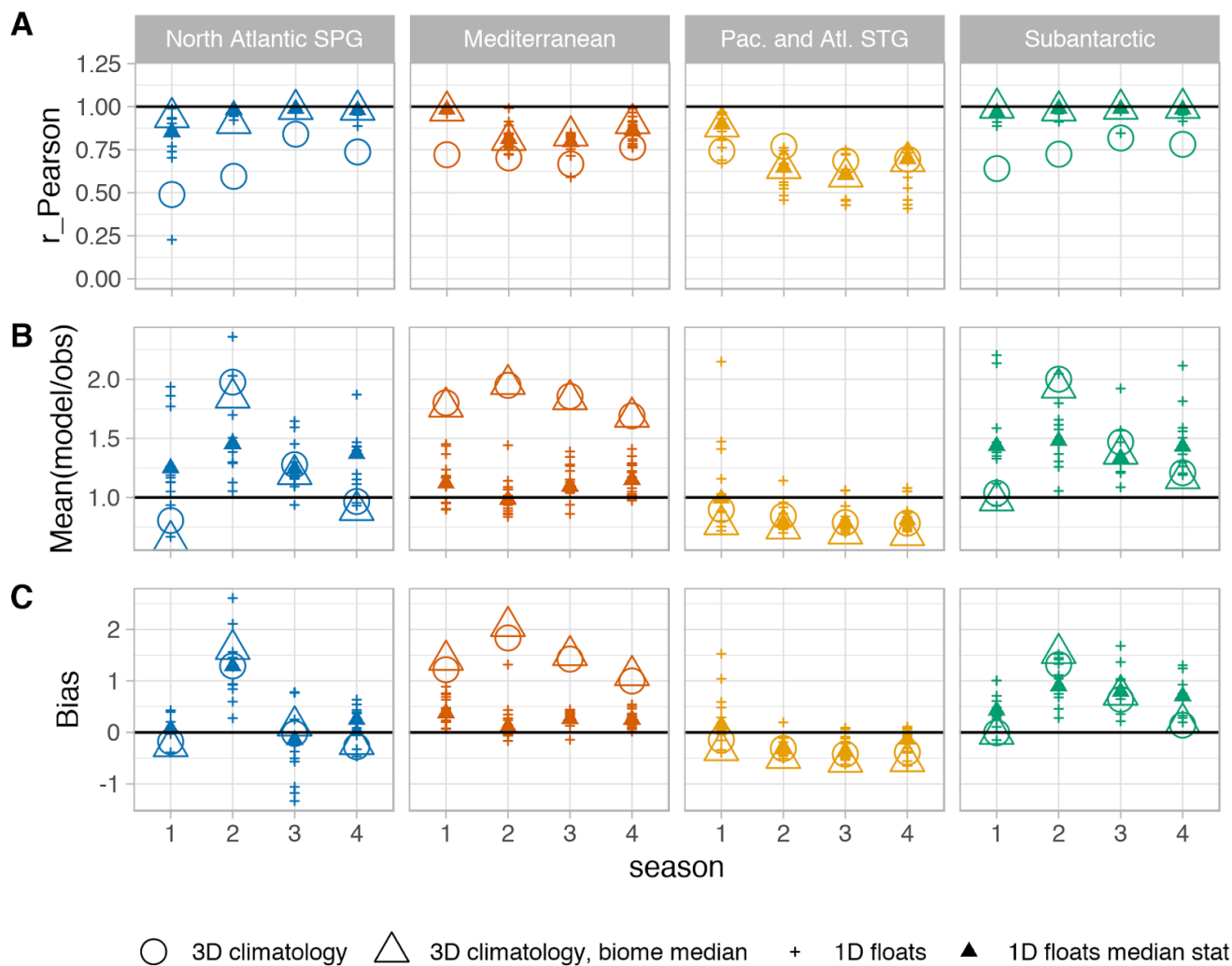
1175



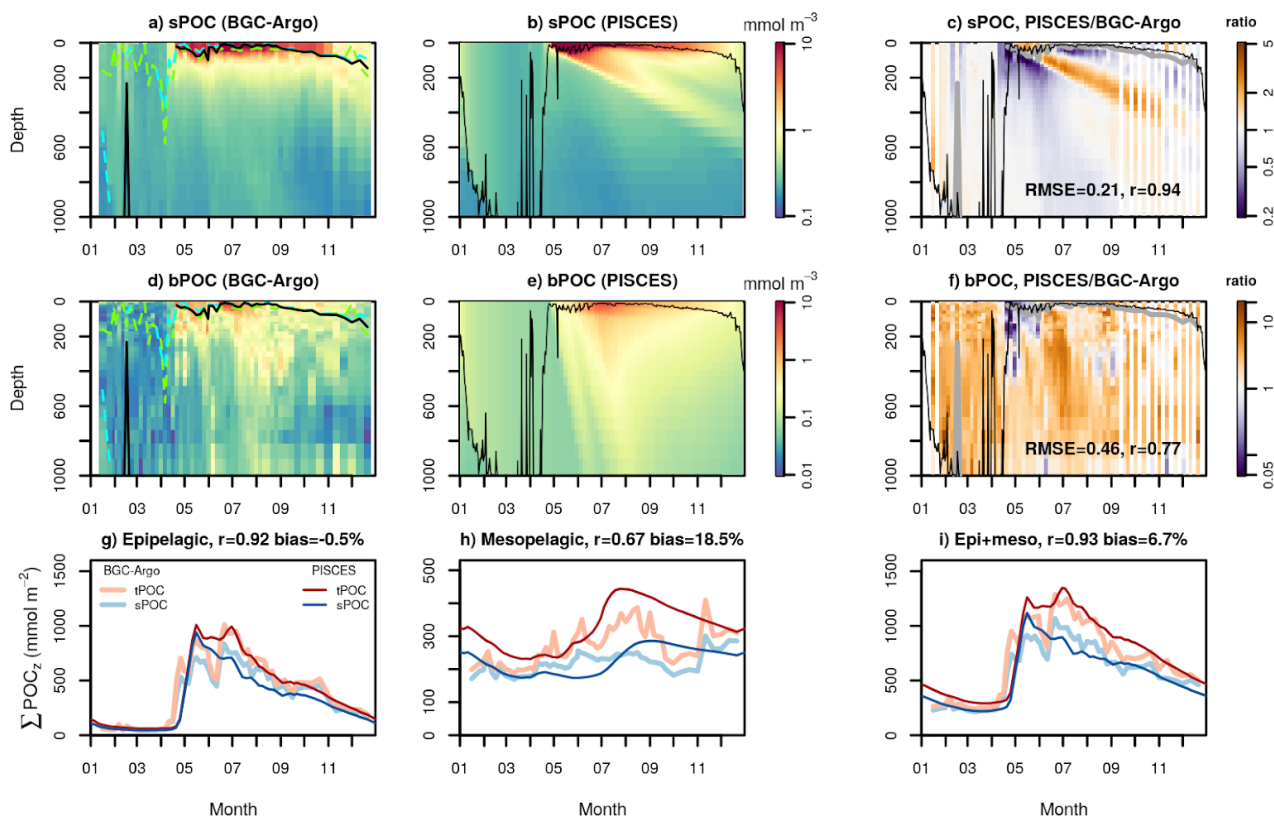
1180 **Figure 3. Monthly sea-surface particulate organic carbon (POC) concentration. Shown are POC estimates based on BGC-Argo (derived from the backscattering coefficient at 700 nm, $bbp700$), satellite (GlobColour) and PISCES. PISCES tPOC results from the addition of the detritus (D), phytoplankton (P) and zooplankton (Z) tracers (Table 1), which are shown here as cumulative sums.**



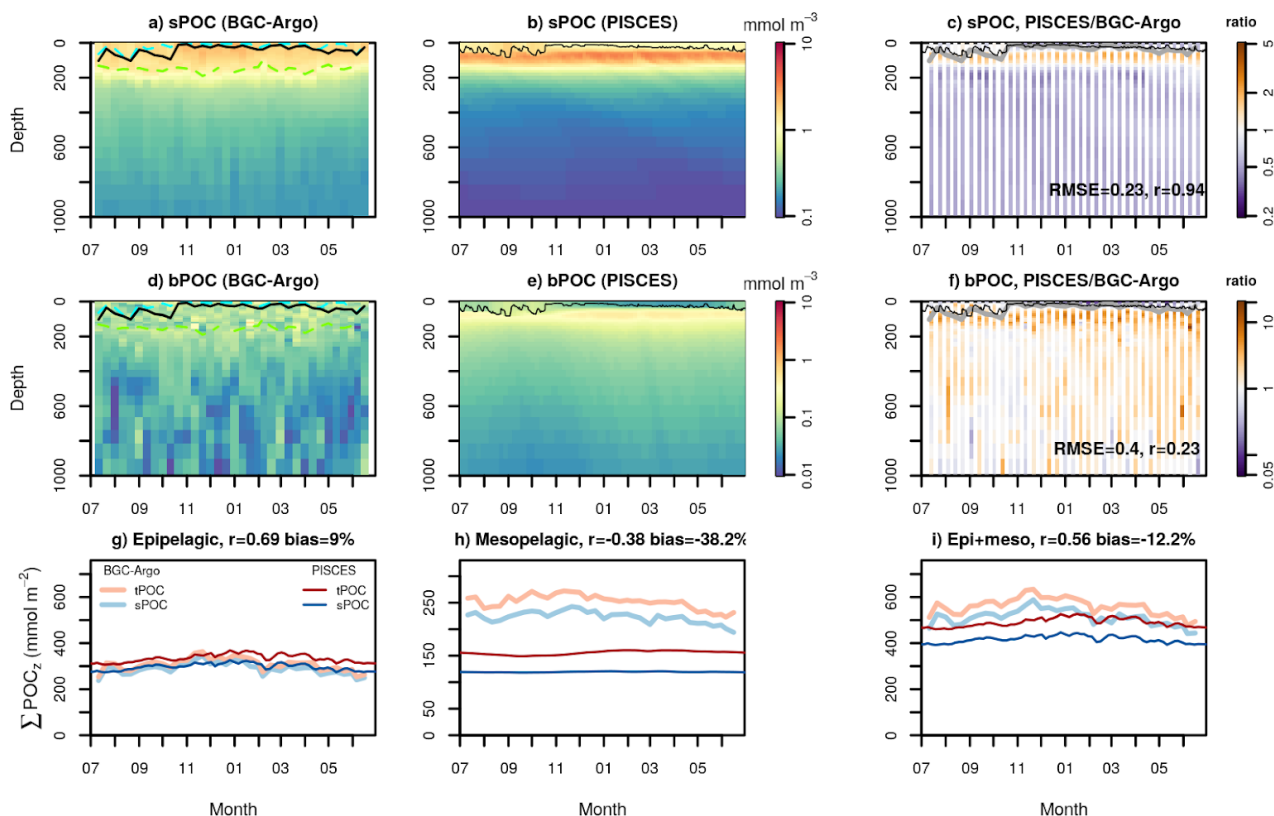
1185 **Figure 4.** Seasonal 0–1000 m particulate organic carbon (POC) profiles. BGC-Argo observations (based on the backscattering coefficient at 700 nm, bbp700) are represented with the median and the 0.025–0.975 quantiles within each biome. PISCES tPOC results from the addition of the detritus (D), phytoplankton (P) and zooplankton (Z) tracers (Table 1), which are shown here as cumulative sums.



1190 **Figure 5. Summary of skill metrics for the comparison between PISCES and BGC-Argo particulate organic carbon (POC) profiles**
in different biomes and seasons. Pearson's correlation coefficient, mean model/data quotient, and mean bias (mmol m^{-3}) are
computed in linear space (untransformed data). Horizontal black lines show the benchmark values for each statistic. Symbols
represent different types of simulations and data aggregation levels. In the case of the PISCES 3D climatological simulation,
 1195 **the statistics are computed at two spatial aggregation levels: using all the grid cells with matching BGC-Argo profiles in a given biome**
(circles); and after averaging all the documented grid cells within the biome (empty triangles), as displayed in Fig. 4. In the case of
the PISCES 1D simulations, statistics are computed for each individual CATS separately (small crosses), and the biome-season
median is also shown (small filled triangles).



1200 **Figure 6.** Temporal evolution of small POC (sPOC) and big POC (bPOC) concentrations in the North Atlantic subpolar gyre
 (NASPG). Panels a and d show observations from the BGC-Argo float WMO 6901486, which drifted in the Labrador Sea during
 the year 2015. Panels b and e show the corresponding PISCES 1D simulation. Panels c and f show the ratio between the model
 and the observations and the corresponding correlation coefficient and RMSE in \log_{10} scale. Solid lines depict the observed MLD (a, d)
 and the simulated turbocline depth (b, e). In panels c and f, the observed MLD is shown in gray to avoid confusion. In panels a and
 1205 d, dashed lines show the depths of the maximum chlorophyll fluorescence gradient (green) and an alternative MLD estimated with
 a 0.005 density threshold to capture weak stratification. The bottom panels show the vertically integrated sPOC and bPOC stocks
 in different layers: 0–200 m or epipelagic (g), 200–1000 m or mesopelagic (g) and 0–1000 m (i). On top of panels g–i we show the
 correlation and bias between BGC-Argo and PISCES total POC (tPOC).



1210

Figure 7. Temporal evolution of small and big POC concentrations (sPOC and bPOC, respectively) in the South Pacific subtropical gyre (STG). Panels a and d show observations from the BGC-Argo float WMO 6901660, which drifted westwards near Tahiti, during the year 2016. Panels b and e show the corresponding PISCES 1D simulation. Panels c and f show the ratio between the model and the observations and the corresponding correlation coefficient and RMSE in log₁₀ scale. Solid lines depict the observed MLD (a, d) and the simulated turbocline depth (b, e). In panels c and f, the observed MLD is shown in gray to avoid confusion. In panels a and d, dashed lines show the depths of the maximum chlorophyll fluorescence gradient (green) and an alternative MLD estimated with a 0.005 density threshold to capture weak stratification. The bottom panels show the vertically integrated sPOC and bPOC stocks in different layers: 0–200 m or epipelagic (g), 200–1000 m or mesopelagic (g) and 0–1000 m (i). On top of panels g–i we show the correlation and bias between BGC-Argo and PISCES total POC (tPOC).

1220

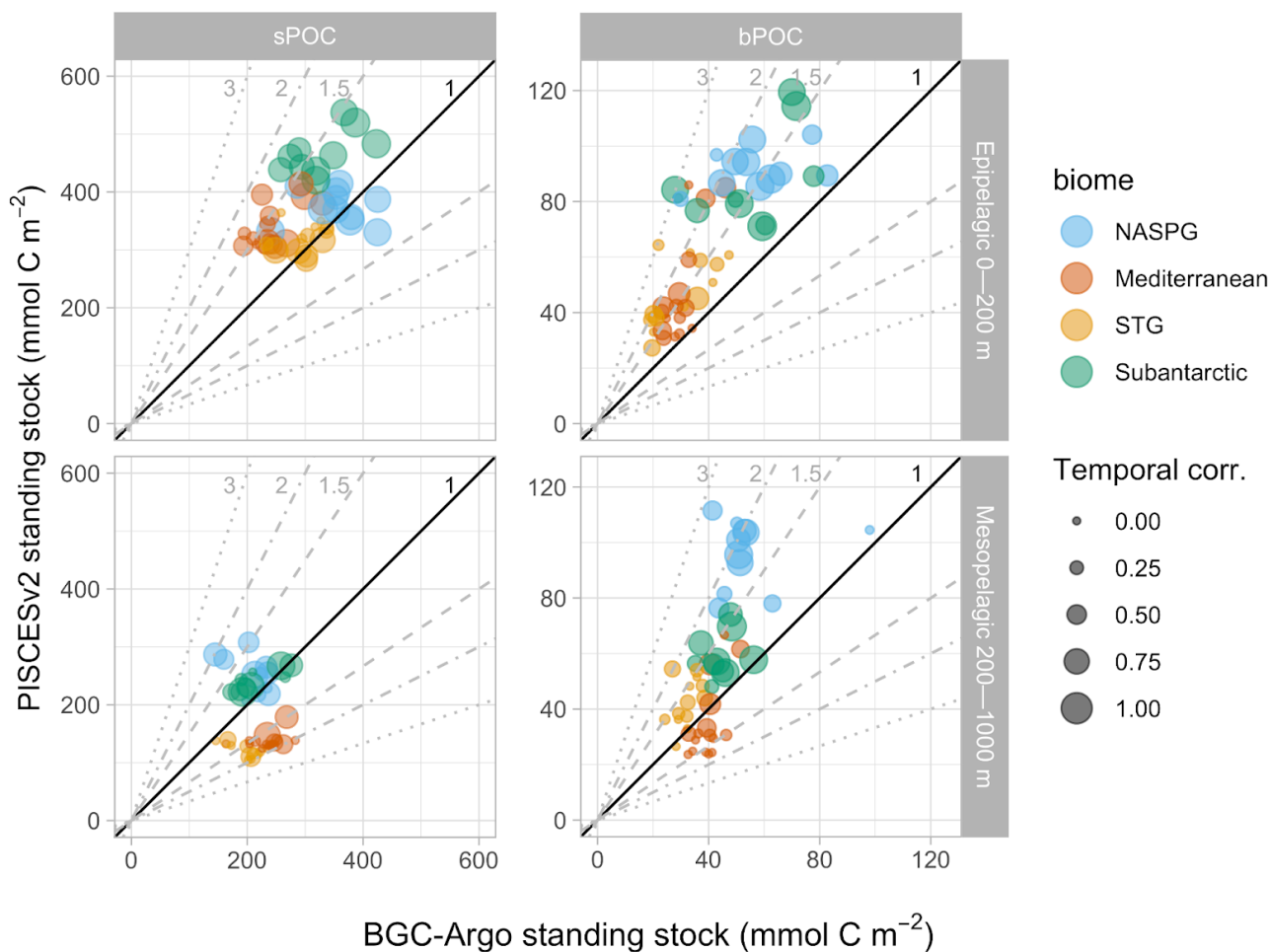
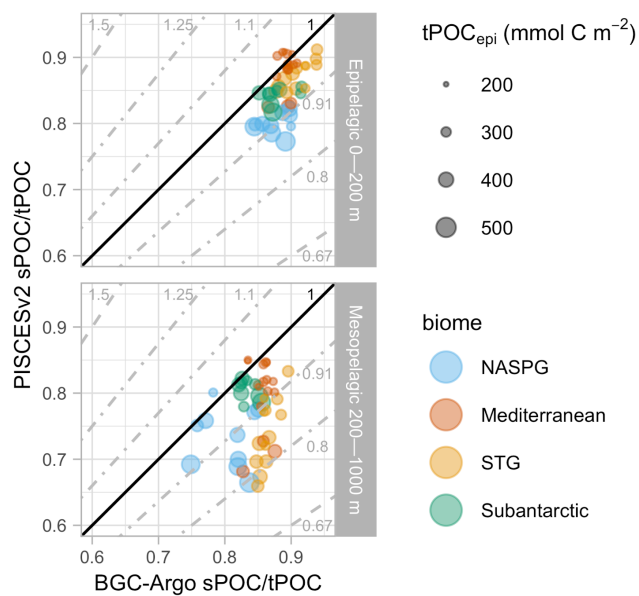
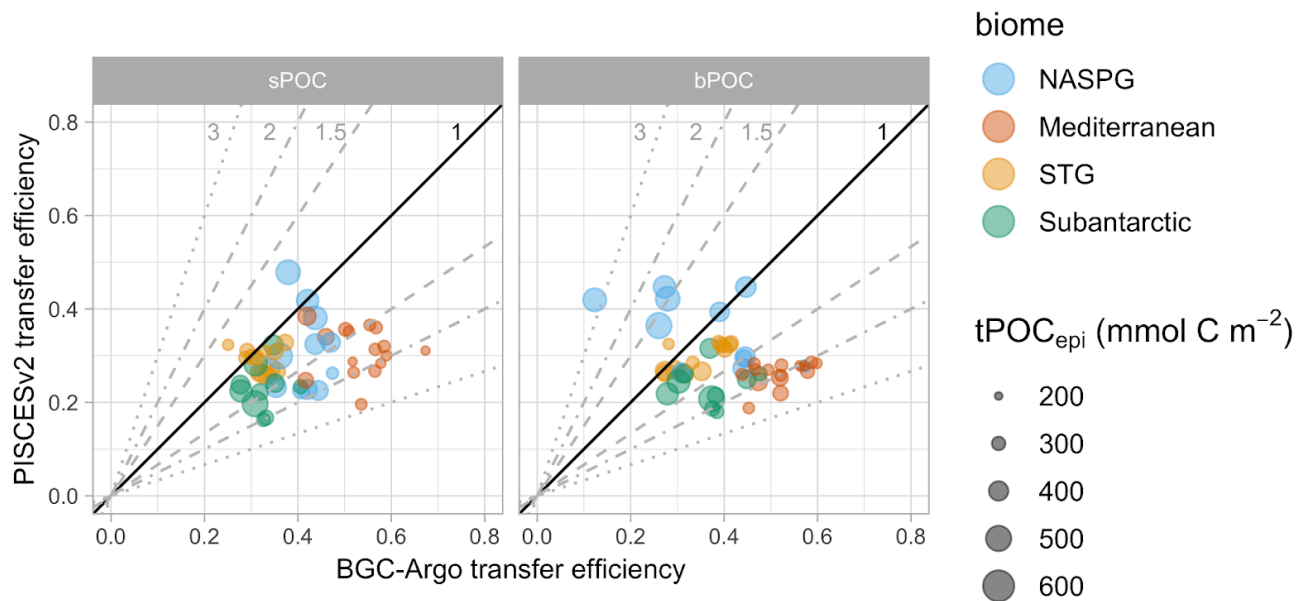


Figure 8. Mean annual POC stocks. BGC-Argo versus PISCES scatterplots are shown for small POC (sPOC) and big POC (bPOC) in the epi- and mesopelagic layers. Reference lines indicate a range of model: data ratios, from 1:1 (perfect correspondence) to a factor of 3 or its inverse. Biomes are distinguished with different colors, and the size of the circles is proportional to the correlation between BGC-Argo and PISCES stocks (as shown in the bottom panels of Figures 6 and 7).

1225



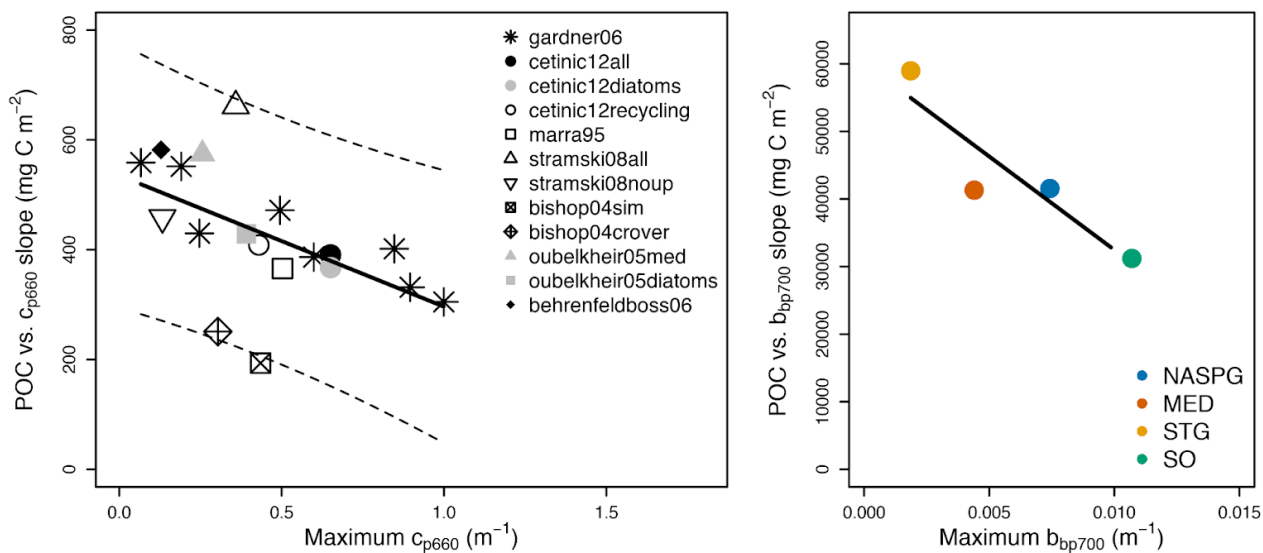
1230 **Figure 9.** Mean annual sPOC/tPOC fractions. BGC-Argo versus PISCES scatterplots are shown for small POC (sPOC) and big POC (bPOC) in the epi- and mesopelagic layers. Reference lines indicate a range of model:data ratios, from 1:1 (perfect correspondence) to a factor of 1.5 or its inverse. Biomes are distinguished with different colors, and the size of the circles is proportional to the annual mean tPOC stock in the epipelagic layer, an indicator of productivity.



1235

Figure 10. Mean annual POC transfer efficiency between 200 and 700 m. BGC-Argo versus PISCES scatterplots are shown for small POC (sPOC) and big POC (bPOC). Reference lines indicate a range of model: data ratios, from 1:1 (perfect correspondence) to a factor of 3 or its inverse. Biomes are distinguished with different colors, and the size of the circles is proportional to the annual mean tPOC stock in the epipelagic layer, an indicator of productivity.

1240



1245 **Figure A1.** Coherent patterns in the conversion factors between POC and bio-optical variables. The left panel reproduces figure 8 from Cetinić et al. (2012), which shows the relationship between the POC versus c_p slope and the maximum c_p in a given dataset. The right panel shows the analogous relationship for b_{bp700} , as used in our study. Linear fits are only illustrative.



Tables
Table 1. Match between BGC-Argo observations, PISCES tracers (Amont et al., 2017), real-world particulate organic carbon pools, and particle size ranges^a.

POC fraction	BGC-Argo observation	PISCES tracer (carbon currency)	Closest real-world correspondence
sPOC	b_{bp700} vertical profiles, despiked signal. Most sensitive to 0.5–30 μm particles (Dall'Olmo et al., 2009; Organelli et al., 2018) Calibrated as POC with Eq. 1 and 2	PHY: “Nanophytoplankton”, includes calcifiers (default fraction 30%). Nominally 1–10 μm . PHY2: Silicifying microphytoplankton. Nominally 10–50 μm . POC: detrital particulate organic carbon. Nominally < 100 μm . In practice, it includes heterotrophic prokaryotes' biomass with current parameter values (see 4.3). ZOO: Microzooplankton. Nominally 10–200 μm .	Picocyanobacteria and non-diatom phytoeukaryotes, generally 0.5–20 μm . Diatoms, between 1.5– μm cells (Vaulot et al., 2008) and mm-scale chains. Mean ESD ^b generally < 50 μm in seawater (Shoerjs et al., 2002; Ciotti et al., 2002; Bricaud et al., 2004). Detrital particles between ~0.2 $^{\circ}$ μm and 100 μm . In practice, measurements may include particle-attached and free-living organisms, viruses, colloids and adsorbed DOC. Microzooplankton. Mostly ciliates and flagellates with size similar to their prey, down to around 2 μm (Calbet 2008) Free-living heterotrophic prokaryotes (bacteria and archaea), < 1 μm .
bPOC	b_{bp700} vertical profiles, spike signal. Particle size between ~100 μm (b_{bp700} spike of $2.3 \cdot 10^{-5} \text{ m}^{-1}$) and ~2 mm (b_{bp700} spike of $8 \cdot 10^{-3} \text{ m}^{-1}$) (Briggs et al., 2020) Calibrated as POC with Eq. 1 and 2	Heterotrophic prokaryotes (BACT): currently not a prognostic tracer in PISCES. Not considered <i>explicitly</i> in this study (see 4.3). GOC: detrital particulate organic carbon. Nominally > 100 μm ZOO2: Mesozooplankton. Includes flux feeders ^d . Nominally 0.2–2 mm.	Detrital particles > 100 μm (aggregates, fecal pellets). Includes attached microbes. Mesozooplankton ^d

^a See Stemmann and Boss (2012) for typical seawater particle size spectra.

^b Equivalent spherical diameter

^c Particles in the 0.2–0.8 μm size range and DOC are retained with variable efficiency by the filters commonly used to determine POC (Cetinić et al., 2012; Graff et al., 2015; Lee et al., 1995; Moran et al., 1999; Strubinger Sandoval et al., 2021).



^d PISCES mesozooplankton represents mostly copepods in the euphotic layer and flux feeders below it. The fraction of flux feeders is diagnosed in PISCES from the proportion between flux feeding rates and total mesozooplankton ingestion rates. By construction, flux feeding becomes the dominant mode of mesozooplankton feeding below the euphotic layer under productive surface waters in PISCES. In reality, a wide variety of feeding strategies and organisms are found in the mesopelagic (Ikenoue et al., 2019; Kjørboe, 2011; Mayor et al., 2020; Stukel et al., 2019).



Table 2. Global and regional POC stocks, concentrations and fractions in different layers as simulated by PISCESv2.

Variable	Depth range (m)	Open-ocean biomes					Global ^d
		Ice	SPSS ^a	STSS ^b	STPS ^c	Equatorial	
Area (%)		6.5	14.3	12.0	46.0	9.2	100
tPOC (Tg C)	0–200	73	281	263	263	154	1590
	200–1000	57	221	173	397	90	1006
	1000–5000	80	274	237	633	144	1438
tPOC (mmol C m ⁻³)	0–200	1.18	2.22	2.57	1.66	1.99	1.85
	200–1000	0.29	0.48	0.44	0.25	0.29	0.33
	1000–5000	0.14	0.18	0.17	0.10	0.13	0.13
sPOC ^e (%)	0–200	72	81	79	89	84	81
	200–1000	75	75	70	79	71	75
	1000–5000	81	80	77	79	75	79
Phyto ^f (%)	0–20	45	45	41	58	49	50
Diatoms ^g (%)	0–20	28	21	14	3	4	14
Detritus ^h (%)	0–20	15	25	31	26	31	24
	0–200	36	43	48	44	50	42
	200–1000	62	67	70	78	78	70

^a Subpolar seasonally stratified



- ^b Subtropical seasonally stratified
^c Subtropical permanently stratified
5 ^d Larger than the sum of biomes because the latter do not include coastal areas.
^e sPOC / tPOC.
^f (*PHY* + *PHY2*) / tPOC.
^g *PHY2* / tPOC.
^h PISCES detritus (*POC*+*GOC*) divided by tPOC. Heterotrophic prokaryotes are *de facto* included.
- 10



Table A1. Compilation of studies that analyzed the relationship between POC and b_{p700} in the euphotic layer of the oceans.

Location	Reference	N	Depth range	Slope (mg C m ⁻² m)	Intercept	Comments
North Atlantic Subpolar Gyre	Cetinić et al., 2012	321	0-600	35422 ± 1754	- 14.4 ± 5.8	Downcast
		321	0-600	43317 ± 2092	- 18.4 ± 5.8	Upcast
	Bol et al., 2018	n.a. ^a	0-10	41550	forced through 0	Subset of Cetinić et al., 2012 at the surface
Mediterranean	Loisel et al., 2001	N/A	N/A	41305	1.43	Original measurements at 555 nm
Subtropical and tropical Pacific and Atlantic (upwellings excluded)	Stramski et al., 2008	54	4-8	58968	2.75	Original measurements at 555 nm
Subantarctic	Johnson et al., 2017	67	0-100	31200 ± 2470	3.0 ± 6.8	

^a n.a. = not available